

## DISCOVERY OF SIX OPTICAL PHASE CURVES WITH *K2*

PRAJWAL NIRLA<sup>1,2</sup>, SETH REDFIELD<sup>2</sup>, JULIEN DE WIT<sup>1</sup>, FEI DAI<sup>3,4</sup>, ISMAEL MIRELES<sup>2</sup>, DILOVAN SERINDAG<sup>5</sup>, AVI SHPORER<sup>3</sup>

<sup>1</sup>Department of Earth, Atmospheric and Planetary Sciences, MIT, 77 Massachusetts Avenue, Cambridge, MA 02139, USA; Corresponding author: pniraula@mit.edu

<sup>2</sup>Astronomy Department and Van Vleck Observatory, Wesleyan University, Middletown, CT 06459, USA

<sup>3</sup>Department of Physics and Kavli Institute for Astrophysics and Space Research, Massachusetts Institute of Technology, Cambridge, MA 02139, USA

<sup>4</sup>Department of Astrophysical Sciences, Peyton Hall, 4 Ivy Lane, Princeton, NJ 08540 USA

<sup>5</sup>Leiden Observatory, Leiden University, P.O. Box 9513, 2300 RA Leiden, The Netherlands

### ABSTRACT

We have systematically searched for the phase curves among the planets discovered by *K2*. Using the reported planetary parameters, we screen out the best potential candidates, and examine their light curves in detail. For our work, we consider light curves from two different detrending pipelines - EVEREST and K2SFF. In order to remove stellar variability and systematics, we test three different filtering techniques: spline, phasma (median-filtering) and Butterworth (harmonics filtering), and use Butterworth filtered light curves for the subsequent analysis. We have identified 6 previously unreported phase curves among the planets observed with *K2*: K2-31b, HATS-9b, HATS-11b, K2-107b, K2-131b, and K2-106b. The first four of these are hot Jupiters for which we find the photometric masses consistent with their RV-based masses within  $2\sigma$ ,  $1\sigma$ ,  $1\sigma$ , and  $3\sigma$  respectively with comparatively low geometric albedos, while the last two are ultra-short period super-Earths with phase curves dominated by reflective and thermal components. We also detect a secondary eclipse in HATS-11b at  $62\pm 12$  ppm. We thus deem it to be possible to validate the planetary nature of selected *K2*, and suggest similar vetting could be used for the ongoing *TESS* mission.

*Keywords:* planetary systems: K2-31b, HATS-9b, HATS-12b, K2-107b, K2-131b, K2-106b, HATS-11b, Qatar-2b, K2-141b, and WASP-104b, – technique: photometric

### 1. INTRODUCTION

Phase curve analysis has established itself as an important tool in characterizing exoplanets. It is commonly used to study close-in massive planets, opening up a window to independently characterize the planetary parameters such as eccentricity, geometric albedo, longitudinal temperature distribution, cloud coverage as well as planetary mass (for a detail review, see Shporer (2017), or Parmentier & Crossfield (2018)). While infrared windows are often ideal for observing the thermal phase curve of planets as planetary emission often peak in such bandpass (e.g. Harrington et al. 2006; Knutson et al. 2007; Adams & Laughlin 2018), the limited number of space based infrared facilities has been the primary bottleneck for such studies. This is where space-based photometric missions such as Convection, Rotation, and planetary Transits (*CoRoT*; Baglin et al. 2002), and *Kepler* (Borucki et al. 2010) have come to play a crucial role through optical phase curves. While leading in the discoveries of the exoplanets, these mission have also signif-

icantly increased the number of phase curve detections. For instance with *Kepler*, photometric time series were obtained for thousands of targets with unprecedented precision. For reference, a combined differential photometric precision of 29.0 ppm was reported for  $K_p = 11.5$  to 12 mag stars in the long cadence mode (Gilliland et al. 2011). This has already led to the discovery of robust phase curves for more than 20 transiting *Kepler* planets (Borucki et al. 2009; Welsh et al. 2010; Batalha et al. 2011; Barclay et al. 2012; Esteves et al. 2015; Angerhausen et al. 2015). Additionally, the precise photometry has been used to estimate RV-independent masses (Faijler et al. 2013; Esteves et al. 2013), validating the planetary nature of transiting objects (Quintana et al. 2013; Sanchis-Ojeda et al. 2013) well as for the discovery non-transiting systems (Faijler et al. 2012; Millholland & Laughlin 2017).

Despite operating only on two reaction wheels, the revamped *K2* mission is able to achieve photometric precision on par with the original *Kepler* mission. This has

been possible not only due to ingenious mission redesign (Howell et al. 2014) but also because of a host of tools that have been developed in response to the unique data challenges caused primarily by, but not limited to, the telescope drift (Vanderburg & Johnson 2014; Luger et al. 2016). Despite *K2*'s relatively short baseline of  $\sim 80$  days (compared to the primary mission's four year baseline), its high precision observation of numerous bright targets ( $V \sim 10$  mag) translates into good opportunities for detecting phase curves.

Yet, there are unique challenges in studying phase curves with a 'short' observation baseline. Not only does the shorter length of observation make it particularly difficult when it comes to disentangling the phase curve from quasi-periodic signals such as those arising from spot modulation, but non-periodic effects such as thermal settling or edge effects will disproportionately distort the final obtained signal. In the case of *K2*, the required aggressive post processing of the data to correct the systematics can also affect the astrophysical signal under consideration. Not to mention, there are gaps in our understanding of the physics behind phase curves. Intriguing questions surrounding the existence and the cause of the third harmonics observed in systems such as HAT-P-7b and Kepler-13Ab still eludes a clear explanation (Shporer et al. 2014; Esteves et al. 2015; Cowan et al. 2017). A handful of the optical phase curves have been observed with significant asymmetries, which have been attributed to scattering due to inhomogeneous clouds (Demory et al. 2013; Shporer & Hu 2015). Meanwhile, Armstrong et al. (2016) measured the temporal variations of the optical phase curve of HAT-P-7b, which comes with the prescription for the climatic variability in planets, thereby undermining the classical picture of a consistent signal present throughout the time series. Similarly, given the small signal amplitude, correlated noise as well as dilution can dramatically affect the inferred conclusions we derive from the phase curves (see discussions surrounding Kepler-91b in Esteves et al. 2013; Lillo-Box et al. 2014). This all points to the complex world of planetary atmospheres hidden under the simple phase curve models, robust characterization of which would require more precise data.

Despite these challenges, there are already three reported planetary phase curves in *K2* data: Qatar 2b (Dai et al. 2017b), K2-141b (Malavolta et al. 2018), and WASP-104b (Močnik et al. 2018). Hot Jupiters like Qatar-2b and WASP-104b have light curves exhibiting ellipsoidal variation and Doppler boosting consistent with their radial velocity (RV) based masses. On the other hand, K2-141b, an ultra short period super-Earth, has a measurable phase curve dominated by reflective and thermal components. As more than 350 planets have been discovered by *K2*, we have under-

taken a project to systematically search for phase curves among the selected *K2* light curves where phase curve detection is feasible.

In §2 of this work, we introduce the process used to screen out the targets for the phase curves among the *K2* planets. In §3, we present the pipeline used to process the data including discussion on different filtering processes, and in §4 we perform Signal Injection and Retrieval test to probe the strengths and weaknesses of our pipelines. Under §5, we discuss the model framework used for the phase curve, and the fitting procedures whereas the results are presented in §6. This is followed by the reportings on secondary eclipse in §7. In §8 and §9, we present the scientific insights gained through our work, which is followed by the conclusion. We present the the light curves used in our data analysis in the Appendix.

## 2. POTENTIAL CANDIDATES

For this study, we have only considered the confirmed exoplanets. Our search included 382 exoplanets which were observed by *K2*, all of which were catalogued in NASA Exoplanet Archive<sup>1</sup> as of December 18, 2018 with the *K2* flag. While the *K2* mission itself has come to an end, the data from the mission is still being processed and discovery numbers are expected to increase as candidates continue to be validated with follow-up observations. Phase curve studies, such as the analysis presented in this paper, can also be applied to other photometric exoplanet surveys such as Transiting Exoplanet Search Survey (*TESS*; Ricker et al. 2015), which is expected to find as many as  $\sim 10^4$  planets primarily in short period orbits (Huang et al. 2018).

As the possibility of the detection of phase curves primarily boils down to the precision of the light curve, we filter out the suitable candidates by estimating the magnitude of the combined signal against the obtainable precision of the light curve. We use the parameters recorded in the database to estimate the equivalent amplitude of the phase curve signal. When some of the values were missing, estimates were made based on other available parameters of the planet. Using the combined amplitude of all four different effects i.e. reflective, thermal, ellipsoidal and Doppler components, we calculate the expected signal to noise ratio using an estimator for the precision of the light curve as below:

$$\begin{aligned} \text{SNR} &= \frac{((A_{Ref} + A_{Th})^2 + A_{Ell}^2 + A_{Dop}^2)^{\frac{1}{2}} \cdot N^{\frac{1}{2}}}{\sqrt{2}\sigma} \\ &= \frac{A_{Eqv} \cdot N^{\frac{1}{2}}}{\sqrt{2}\sigma} \end{aligned} \quad (1)$$

<sup>1</sup> <https://exoplanetarchive.ipac.caltech.edu>

where  $N$  is the number of observed photometric points set to 3500 (roughly 30 minutes bin over 80 days observation period), and  $\sigma$  is the precision expected to be determined by the brightness of the target in *Kepler* bandpass using pre-flight estimates. The equivalent amplitude is considered to be the amplitude of the sinusoidal signal which has power equivalent to the combined elements of the phase curve:

$$A_{Eqv} = ((A_{Ref} + A_{Th})^2 + A_{Ell}^2 + A_{Dop}^2)^{\frac{1}{2}} \quad (2)$$

To estimate the reflective component ( $A_{Ref}$ ), we assume the geometric albedo ( $A_g$ ) of 0.4 and evaluate the reflective component ( $A_{Ref}$ ) as follows:

$$A_{Ref} = A_g \left( \frac{R_p/R_*}{a/R_*} \right)^2, \quad (3)$$

where  $R_p/R_*$  is the scaled radius of the planet, and  $a/R_*$

is the scaled semi-major axis. Similarly, the thermal variation ( $A_{Th}$ ) is calculated as:

$$A_{Th} = \left( \frac{R_p}{R_*} \right)^2 \frac{\int B(T_{Day})R(\lambda)d\lambda}{\int B(T_*)R(\lambda)d\lambda}, \quad (4)$$

where  $B(T)$  is the Planck's black body radiation law corresponding to temperature  $T$ ,  $R(\lambda)$  is the response function of *Kepler/K2*, and  $T_{Day}$  is the day-side temperature of the planet, which is estimated as following:

$$T_{Day} = T_{eff} \sqrt{\frac{1}{a/R_*} [f(1 - A_B)]^{\frac{1}{4}}}, \quad (5)$$

where  $T_{eff}$  is the effective temperature of the host star,  $A_B$  is the Bond albedo set at 0.6 following a Lambertian sphere relation ( $A_B = \frac{3}{2}A_g$ ), and  $f$  is a proxy variable for re-circulation set at 2/3 corresponding to the case where only the day-side is re-radiating (López-Morales & Seager 2007).

**Table 1.** All *K2* targets analyzed for the phase curves with various relevant parameters.

Identifier	EPIC ID	Kp (Mag)	Campaign	Period (Days)	$R_p/R_*$	$A_{Ref}$	$A_{Th}$	$A_{Ell}$	$A_{Dop}$	$A_{Eqv}$	SNR
<b>K2-31b</b>	204129699	10.6	2	1.258	0.135	199.2	1.4	11.9	4.7	201	228.9
WASP-85 Ab	201862715	10.3	1	2.656	0.163	144.5	0.80	2.2	2.1	145	200.2
K2-237b	229426032	11.5	11	2.181	0.118	184.1	5.8	8.8	2.4	190	132.9
HAT-P-56b	202126852	10.9	0	2.791	0.105	109.5	3.0	7.0	2.8	113	109.3
<b>WASP-104b<sup>a</sup></b>	248662696	11.6	14	1.755	0.121	138.4	0.9	5.8	2.7	140	91.9
<b>QATAR-2b<sup>b</sup></b>	21275629	13.0	6	1.337	0.162	247.6	0.4	18.5	8.3	249	65.1
K2-183b	211562654	12.8	5	0.469	0.027	152.8	50.6	1.9	0.0	203	63.2
WASP-75b	206154641	11.8	3	2.484	0.103	103.8	1.7	4.2	1.7	106	61.8
WASP-118b	220303276	10.9	8	4.046	0.082	59.9	1.2	1.5	0.6	61	58.1
K2-260 b	246911830	12.5	13	2.627	0.097	135.3	5.3	7.9	1.9	141	52.9
K2-34b	212110888	11.4	5, 16	2.996	0.088	65.5	0.9	6.3	2.5	67	47.3
<b>K2-141b<sup>c</sup></b>	246393474	10.6	12	0.280	0.020	31.6	2.4	2.8	0.1	34	38.6
<b>HATS-9b</b>	217671466	13.1	7	1.915	0.083	145.5	3.7	13.6	1.8	150	37.0
WASP-28b	246375295	11.9	12	3.407	0.116	69.7	0.4	1.5	1.4	70	36.9
K2-266b	248435473	11.4	14	0.659	0.043	46.2	0.4	1.1	0.2	47	34.2
WASP-55b	212300977	11.7	6	4.466	0.125	52.4	0.1	0.5	0.8	53	32.2
<b>K2-107b</b>	216468514	12.8	7	3.314	0.083	83.3	1.8	4.1	1.1	85	26.6
WASP-47b	206103150	11.8	3	4.161	0.102	44.1	0.1	1.6	1.8	44	25.9
<b>HATS-12b</b>	218131080	12.7	7	3.143	0.063	73.2	4.2	17.8	2.8	79	25.6
WASP-107b	228724232	11.2	10	5.721	0.145	25.5	0.0	0.0	0.3	26	20.4
K2-29b	211089792	12.9	4	3.259	0.142	72.9	0.7	0.9	1.4	73	20.4
HD 3167b	220383386	9.0	8	0.957	0.017	7.3	1.4	0.4	0.0	7.5	19.3
K2-39b	206247743	10.6	3	4.605	0.019	12.7	0.4	5.0	0.2	14	16.4
HATS-11b	216414930	13.7	7	3.619	0.107	97.1	1.2	3.1	1.3	98	15.5
K2-267b	246851721	11.3	13	6.180	0.0681	19.3	0.1	0.1	0.1	19	15.3

Table 1 continued

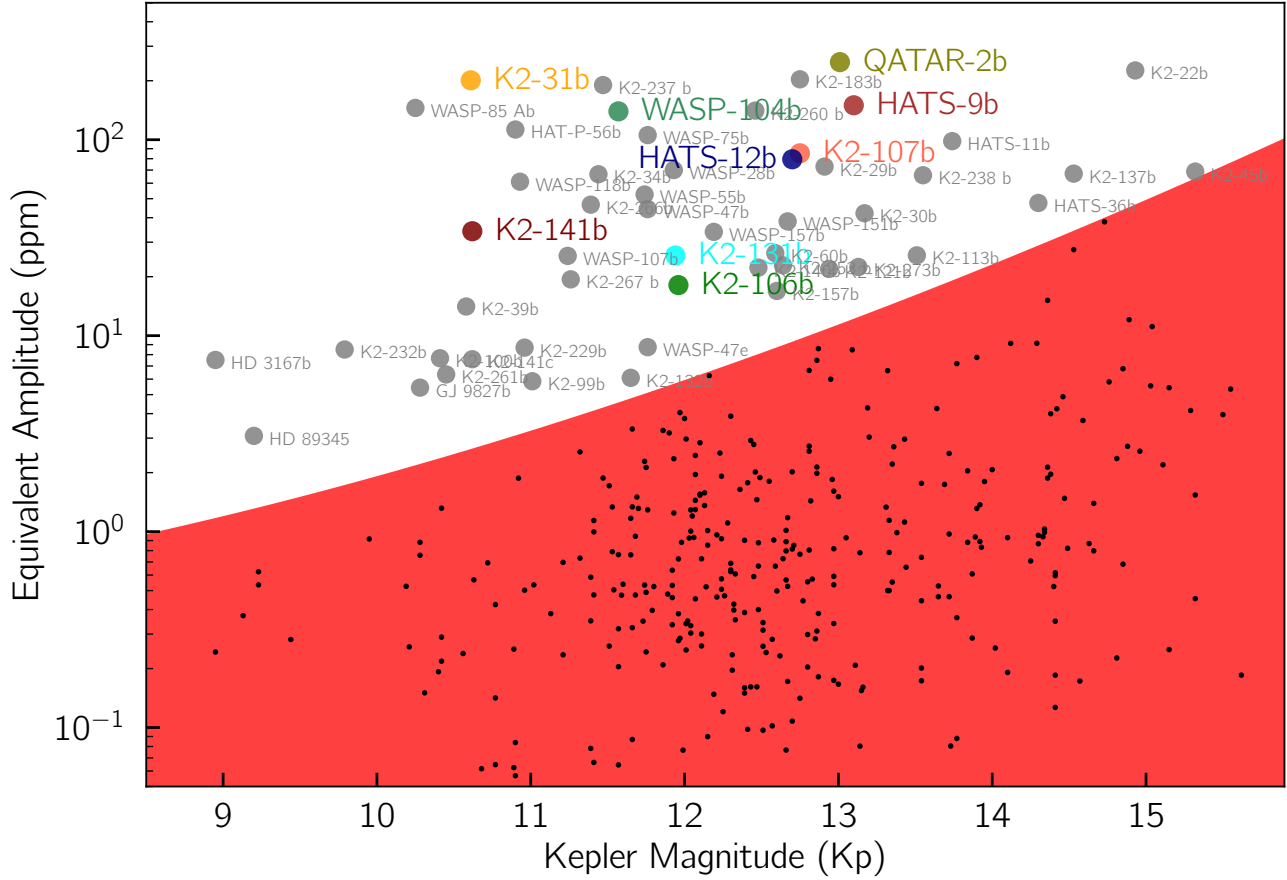


**Figure 1.** Expected signal amplitude ( $A_{eqv}$ ) versus the *Kepler* magnitude for the *K2* detected planets. The red region contains the planet for which SNR detection is expected to be less than  $3\sigma$ . Out of 382 planets, 52 could have detectable phase signal above  $3\sigma$  level and are listed in Table 1. Among these, 9 planets have detected phase curves, all of which are drawn in colors other than grey to improve the readability of the graph.

Table 1 (continued)

Identifier	EPIC ID	Kp (Mag)	Campaign	Period (Days)	$R_p/R_*$	$A_{Ref}$	$A_{Th}$	$A_{EU}$	$A_{Dop}$	$A_{Eqv}$	SNR
WASP-157b	212697709	12.2	6	3.952	0.094	33.8	0.1	0.5	0.8	34	15.2
K2-232b	247098361	9.79	13	11.168	0.020	8.5	0.0	0.1	0.4	8.5	14.8
K2-22b	201637175	14.9	1	0.381	0.075	205.8	1.8	87.7	9.0	226	14.5
<b>K2-131b</b>	228732031	11.9	10	0.369	0.020	23.5	2.1	1.8	0.1	26	13.5
WASP-151b	246441449	12.7	12	4.533	0.101	38.2	0.1	0.3	0.4	38	12.6
K2-238 b	246067459	13.6	12	3.205	0.080	65.1	0.6	3.8	1.3	66	11.8
K2-30b	210957318	13.2	4	4.100	0.127	42.1	0.0	0.5	1.0	42	9.9
K2-100b	211990866	10.4	5	1.674	0.027	7.5	0.1	0.1	0.0	7.7	9.7
<b>K2-106b</b>	220674823	12.0	8	0.571	0.017	16.3	1.7	2.0	0.1	18	9.4
K2-60b	206038483	12.6	3	3.003	0.063	26.2	0.1	1.2	0.8	26	9.1
K2-141c	246393474	10.6	12	7.749	0.094	7.6	0.0	0.0	0.0	7.6	8.6
K2-140b	228735255	12.5	10	6.569	0.114	22.2	0.0	0.4	1.4	22	8.3
K2-229b	228801451	11.0	10	0.584	0.014	8.2	0.5	0.4	0.0	8.7	8.2
K2-261b	201498078	10.5	14	11.633	0.053	6.3	0.0	0.1	0.2	6.3	7.9

Table 1 continued

Table 1 (*continued*)

Identifier	EPIC ID	Kp (Mag)	Campaign	Period (Days)	$R_p/R_*$	$A_{Ref}$	$A_{Th}$	$A_{Ell}$	$A_{Dop}$	$A_{Eqv}$	SNR
K2-253 b	228809550	12.6	10	4.002	0.105	22.8	0.0	0.0	0.1	23	7.7
GJ 9827b	246389858	10.3	12	1.209	0.025	5.4	0.0	0.1	0.1	5.4	7.4
HD 89345	248777106	9.2	14	11.814	0.038	3.1	0.0	0.1	0.1	3.1	7.0
K2-121b	211818569	12.9	5	5.186	0.109	21.9	0.0	0.0	0.1	22	6.0
K2-137b	228813918	14.5	10	0.180	0.018	17.0	0.2	64.7	5.1	67	5.8
K2-157b	201130233	12.6	10	0.365	0.011	13.9	2.9	1.8	0.0	17	5.8
K2-273b	211919004	13.1	5,16,18	11.716	0.0484	22.3	0.1	0.2	0.0	22	5.4
K2-99b	212803289	11.0	6,17	18.249	0.042	5.8	0.0	0.5	0.7	5.9	5.3
WASP-47e	206103150	11.8	3	0.790	0.014	8.1	0.6	1.0	0.1	8.7	5.1
HATS-36b	215969174	14.3	7	4.175	0.110	47.2	0.1	3.1	4.2	48	4.9
K2-113b	220504338	13.5	8	5.818	0.091	25.6	0.0	1.1	1.8	26	4.7
K2-132b	228754001	11.7	10	9.175	0.033	5.9	0.0	1.1	0.6	6.1	3.8
K2-45b	201345483	15.3	1	1.729	0.138	69.1	0.0	0.1	0.2	69	3.3

References for optical phase curves in (a) Močnik et al. (2018), (b) Malavolta et al. (2018), and (c) Dai et al. (2017b)

† All the detected phase curves planets are highlighted in bold.

For calculating the amplitude of the ellipsoidal variation  $A_{Ell}$ , we consider the formulation presented in Morris (1985):

$$A_{Ell} = \alpha_{Ell} \frac{M_p}{M_*} \left( \frac{1}{a/R_*} \right)^3 \sin^2 i, \quad (6)$$

$$\alpha_{Ell} = \frac{0.15(15+u)(1+g)}{(3-u)}, \quad (7)$$

where  $\alpha_{Ell}$  is a constant characterizing tidal distortion,  $M_p$  is the mass of the planet,  $M_*$  is the mass of the star,  $a/R_*$  is the scaled semi-major axis,  $i$  is the inclination of the orbit,  $u$  is the linear limb-darkening parameter, and  $g$  is the gravity-darkening parameter. We determine the value of  $u$  and  $g$  by linearly interpolating among effective temperature, metallicity and  $\log g$  and assuming turbulence of  $2 \text{ km s}^{-1}$  from the table provided by Claret & Bloemen (2011).

Similarly, the Doppler beaming effect ( $A_{Dop}$ ) is modeled as following:

$$K = \left( \frac{2\pi G}{P} \right)^{1/3} \frac{M_p \sin i}{M_*^{2/3} \sqrt{1-e^2}}, \quad (M_p \ll M_*) \quad (8)$$

$$A_{Dop} = \alpha_D \frac{K}{c}, \quad (9)$$

where  $G$  is the gravitational constant,  $P$  is the period,  $M_p$  is the mass of the planet,  $M_*$  is the mass of the star.  $\alpha_D$  is Doppler boosting factor, which is based on the proposition of Loeb & Gaudi (2003). For this work we use the empirical relation reported by Millholland

& Laughlin (2017) between the Doppler boosting coefficient ( $\alpha_D$ ) and effective stellar temperature ( $T_{eff}$ ):

$$\alpha_D = 7.2 - (6 \times 10^{-4})T_{eff}. \quad (10)$$

Table 1 lists 52 *K2* exoplanets arranged in the order of expected signal to noise for phase curve. It also lists the expected individual contributions of all four phase curve components in parts per million (ppm), along other fundamental parameters and information. Figure 1 displays predicted phase curve amplitudes ( $A_{Eqv}$ ) as a function of stellar magnitude. Note that while we expect the ellipsoidal variation and Doppler amplitude to be well constrained around our predicted values, the reflective and thermal components can differ by more than an order of magnitude, depending on the choice of albedo. The choice of high geometric albedo is motivated primarily to cast a wide enough net not to miss any potential candidates. This in turn leads to a high non-detection rate. Additional factors that lead to decreased precision include crowding, imperfect detrending, stellar activity, and other various systematics. Besides, we find that the pre-flight estimates systematically overpredicts the precision for the brighter targets as can be seen in Figure 2. We trace this back to the use of constant aperture size across all targets.

### 3. DATA PREPARATION

Phase curves signals are often times weak compared to other astrophysical signals present in the photometric

time series. Filtering processes to remove them is therefore a necessary step. By the time the final light curve is obtained, the data goes through multiple processing steps, each of which handles different aspects of the systematics. The official *Kepler* processing tool handles many of the detector and electronic effects (Jenkins et al. 2010). However, the pointing induced errors historically have been left up to the exoplanet community to address.

As a response, different pipelines were developed by research groups who have diverse research foci. For instance, Kepler Asteroseismic Science Operations Center (KASOC; Handberg & Lund 2014) pipeline was purposed for astero-seismic related studies, whereas for those interested in the stellar rotational period developed independent pipelines (Angus et al. 2016). Similarly, specialized pipelines have been developed to find transits. For our work we consider two different pipelines, K2SFF (Vanderburg & Johnson 2014; Vanderburg et al. 2016) and EVEREST (Luger et al. 2016, 2018) primarily due to their ability to produce light curves with high precision. For our work, we have used the scatter of the phase folded light curve as the benchmark for selection criterion for any subsequent analysis. This was motivated by the reasoning that systematics is the single-handedly the most challenging hurdle standing in the way of the phase curve detection.

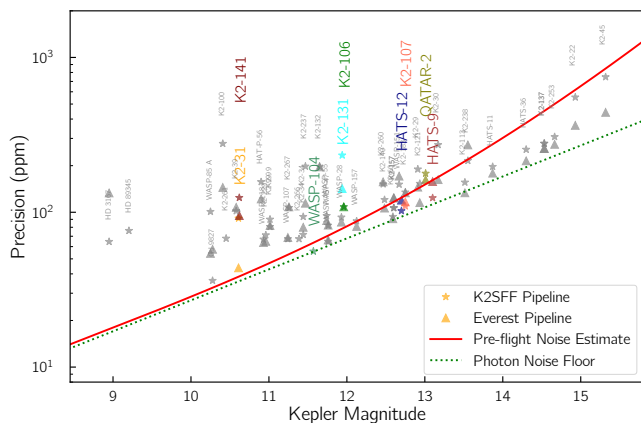


**Figure 2.** The observed precision for our targets compared to the expected noise level used for SNR estimation. The expected noise level underestimates the scatter for bright targets while generally overestimates the noise for the dimmer targets.

### 3.1. Detrending

Due to drift of the field in the rolling axis, which was periodically compensated for by thruster firings, pre-detrended light curves from *K2* exhibit a characteristic sawtooth pattern. Pipelines such as EVEREST, and K2SFF have been designed to remove these and other system-

atics unique to the *K2* data. We particularly focus on using these two pipelines due to their comprehensiveness and the quality of the final products delivered by these pipelines. K2SFF light curves are available for all of our targets, whereas EVEREST is available for all of targets up until Campaign 13 at the time of this publication. All the data is publicly available from the MAST archive.<sup>2</sup>

K2SFF is a parametric approach to detrending - decorrelating the motion of the centroid with the variation of the magnitude. On the other hand, EVEREST is a Gaussian process based detrending which models the intrapixel variation to produce the final light curve. Both of the methods produce light curves that are comparable in photometric precision (see Figure 2). Unfortunately, a comprehensive quantitative comparisons on the performance of these pipelines is beyond the scope of this paper. Light curves from both pipelines have been used successfully in different analyses. Dai et al. (2017b) used the light curve generated by EVEREST pipeline due to its higher precision whereas Malavolta et al. (2018) and Močnik et al. (2018) used some variation of K2SFF in producing the final light curves, which were then used for subsequent phase curve analyses.

The detrending removes most of the power injected at higher frequencies such as those introduced by thruster firing events ( $\sim 6$  hours), while at lower frequencies ( $> 15$  days) other long term systematics still can dominate (Van Cleve et al. 2016; Aranzana et al. 2018). Since the phase curve signals lie in the region ( $\sim 1$  to 5 days) which is usually well separated in the frequency domain from both of these effects, they are minimally distorted, and the treatment by these pipelines are sufficient in most of the cases. However, there are cases where these traditional *K2* pipelines often tend to fail, such as in crowded fields or for bright targets. This in turn has motivated the development of more specialized pipelines to handle crowding typically in a cluster environment (Librato et al. 2016) or bright targets that can saturate the pixels (White et al. 2017). Unfortunately, the light curves from these specialized pipelines are not as comprehensively available for most of *K2* targets, therefore we limit our analysis with the light curves available from EVEREST and K2SFF.

In Figure 2, we compare the observed precision of the light curve against the expected precision. We found that the pre-flight prediction provided for *Kepler* targets<sup>3</sup> overestimates the precision for the brighter targets, whereas it underestimates the precision for the fainter targets. This error can be traced to the constant read

<sup>2</sup> [https://archive.stsci.edu/k2/data\\_search/search.php](https://archive.stsci.edu/k2/data_search/search.php)

<sup>3</sup> <https://keplergo.arc.nasa.gov/CalibrationSN.shtml>

noise error assigned to all of the targets calculated by assuming an aperture size of 20 pixels. For the bright targets the non-linear effects and background contamination poses worse problems than this calculation allows for. While a separate algorithm for detrending bright stars has been explored (White et al. 2017), there might be room for even more optimization. But overall, the assumed precision curve provides a good estimate of the precision expected for our targets.

### 3.2. Outliers Handling

The final light curve obtained by the pipelines needs further processing due to the presence of outliers. We initially remove all the data lying outside eight times the inter-quartile (Q3-Q1) range from the median. Following this, we mask out all the transit points found using the transit parameters reported in the NASA exoplanet database. We then locate the outliers through an iterative spline fitting process by excluding data that lie more than  $3\sigma$  away in each iteration. This process is repeated once the light curve is folded, during which outliers occurring during transit events are removed. On average, this led to removal of around 2.5% of the original data across our targets.

Some of our targets show effects akin to thermal settling at the beginning of the data (see Figure 3). However, since these effects are not uniformly present in all our targets, we did not exclude these data points in our analysis. If multi-campaign observations were available for a target, we combined all of the light curves available to produce the final light curve. *K2* light curves often have a gap typically of a few days at the middle of the observation for data downlinking. These discontinuities are expected and well handled by the detrending pipelines as well as the filtering. For HATS-12 however, there is an abrupt offset at the middle of the observation (see Figure 3) which was observed in both of the detrended light curves. We correct for this apparent offset by modeling the continuum using linear regression at the break point, and applying the relevant offset to generate the final stellar continuum before filtering.

## 4. SIGNAL INJECTION RETRIEVAL TEST

In order to extract the phase curve, the stellar continuum has to be modeled out. A host of filtering techniques have been used in the past. Sometimes the stellar continuum exhibits little to no variation, therefore requiring minimal pre-processing as in the case of TRES-2b (Barclay et al. 2012). However, for most of *K2* targets, filtering provides an opportunity not only to remove the stellar continuum, but also any uncorrected systematics. Thus, we explored suites of filtering techniques available to us, among which we focused particularly on three: spline, phasma and Butterworth. Before

performing all three filtering processes, we masked the region where the primary transit and secondary eclipse. This can lead to increased scatter around the region surrounding occultation. Below we discuss the three filtering techniques, whose performances were evaluated using  $\chi^2_\nu$  as the primary metric:

1. **Spline Filtering:** Spline flattening is the most commonly used filtering technique for removing the stellar flux (Esteves et al. 2013; Shporer & Hu 2015; Angerhausen et al. 2015; Armstrong et al. 2016). Use of different degrees of polynomial or knotting intervals are common depending on the planetary period as well as the ability of the spline to model the stellar continuum. Splines essentially act as a low pass filter, and have been successfully used in a range of targets in the past. For this work, we adopt third degree polynomial knotted once every period of the planet.
2. **Phasma:** Phasma as a filtering method in the context of the phase curve was proposed in Jansen & Kipping (2018). Phasma in essence is a median filtering with window length set to the period of the planet. A similar implementation with a mean filter was also used. While easy to implement, phasma did not perform on par with other filtering techniques particularly among hot Jupiters (see Figure 4 and Figure 5).
3. **Frequency filtering:** Another method that has been used is harmonics based filtering (Quintana et al. 2013). In this work, we use the sixth order Butterworth filter as implemented in `scipy`<sup>4</sup> with a bandpass between half the planetary frequency and 3.5 times the planetary frequency. The limits of the bandpass were partially motivated to preserve the third harmonics (Esteves et al. 2015), as well as decided through trial and error. Before filtering, we uniformly and linearly interpolate the light curve after masking the transit and occultation points. Overall, the performance of Butterworth filter performance was superior among the three filtering techniques studied in detail, particularly among the hot Jupiters (see Figure 4, and Figure 5). However, structural features such as ringing artifacts were more prominent in the residuals.

<sup>4</sup> `scipy.org`

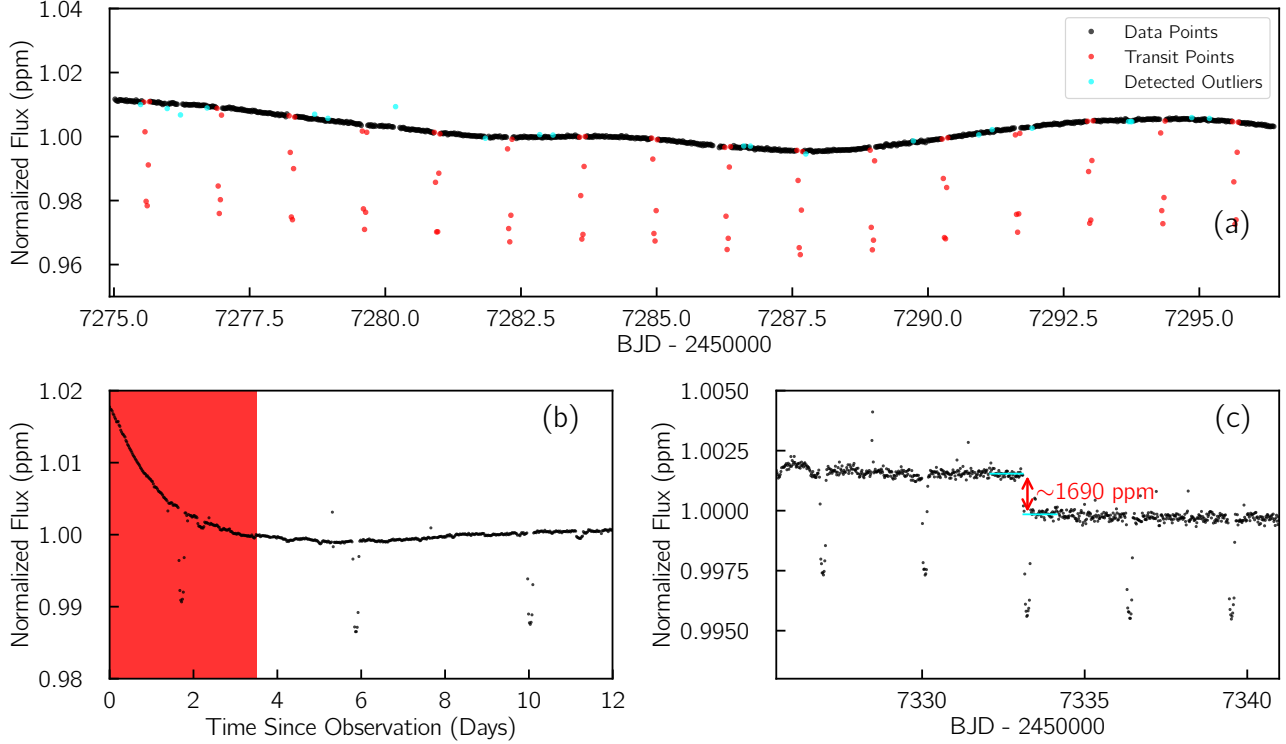


**Figure 3.** Figure showing different systematics in the detrended data. (a) Transit points and outliers detected in a portion of QATAR-2 EVEREST detrended light curve. (b) Potential systematic effects akin to thermal settling observed during the first few days of detrended WASP-47 EVEREST detrended data. (c) An abrupt change is observed in EVEREST detrended data for HATS-12b possibly due to a change in pixel responsivity. Note that a similar offset is spotted in K2SFF detrended data.

**Table 2.** Targets used for Signal Injection Test

Identifier	EPIC IDs
<b>K2-31b</b>	203089855, 203526723, 203758400, 204254456, 204529573
<b>HATS-9b</b>	214576141, 214963629, 215327780 215496957, 216068131
<b>HATS-12b</b>	215293111, 215310931, 215517702 215594041, 215677034
<b>K2-107b</b>	214402646, 215075353, 215542349 215771782, 215834357
<b>K2-131b</b>	201094825, 201094970, 201121210 201141186, 201164625
<b>K2-106b</b>	220197918, 220205426, 220209263 220228282, 220249101

For each system with detected phase curves, we download K2SFF and EVEREST detrended light curves of five target stars from the same campaign with similar magnitude and precision range after detrending. During the process of choosing the light curves for signal injection

test, targets exhibiting strong short term modulation (i.e. less than 10 days), exhibiting intrinsic variability, or having obvious uncorrected systematics were deliberately avoided. The list of targets used for signal injection-retrieval test are reported in Table 2. For the hot Jupiters among our targets, we injected the phase curve signals in the corresponding light curves considering geometric albedos between 0.01 to 0.66 at a step-size of 0.01 and masses between 0.25 and 7.0  $M_{\text{Jup}}$  with a step-size of 0.25  $M_{\text{Jup}}$  while using the reported transit parameters for the planets. We ran the subsequent light curves through our pipeline, and compared the final retrieved signal to the injected phase curve signal. The quick fits using Levenberg-Marquardt minimization showed that in most cases consistent parameters of albedo and mass to the injected signals can be retrieved. During these tests, we found the Butterworth filter outperforms both spline and phasma filtering among hot Jupiters (see Figure 4 and Figure 5). We also performed additional tests with phase offset signals, and Butterworth filter continued to outperform other two filters. For the ultra-short period super-Earths, we performed tests using parameters of K2-141, K2-131 and K2-106 for which we simulate phase curves with a reflective component with geometric albedo ranging between 0.01 to

0.8. For these latter set of planets, the performances of the different filtering techniques were comparable (see Figure 5).

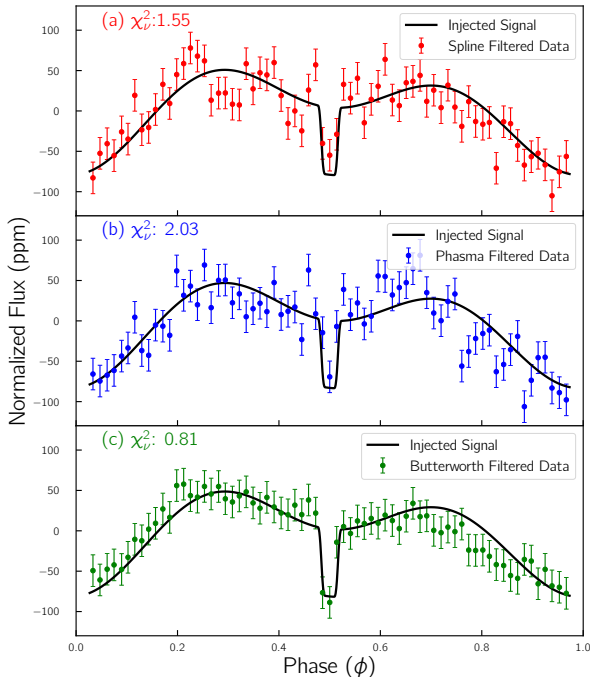


**Figure 4.** A random case of injected signal retrieved through (a) Spline Filtering, (b) Phasma Filtering (c) Butterworth bandpass Filtering. The error bars were scaled down accordingly to the bin-size from the calculated mean scatter.

Based on these tests, we have used Butterworth filtered light curves for all our hot Jupiter targets. The sixth order Butterworth filter allows us to isolate power from a specific frequency band but it can sometimes lead to ringing effects in the residuals visible for some of our targets. Such artifacts were also observed in our injection retrieval test, however presence of these artifacts did not appear to affect the accuracy of the retrieved parameters. We explored the possibility of using narrower bandpass Butterworth filters, however, such implementations tended to decrease the accuracy of the retrieved parameters in our signal injection test. For the short period rocky planets (period less than a day) such as K2-141b, K2-131b or K2-106b, spline flattening light curves were used as its performance is comparable to Butterworth filter, and have already been shown to work robustly on a number of occasions.

Note that our injection-retrieval test has been heavily influenced by the parameters of the systems where we discovered the phase curves. We performed our test

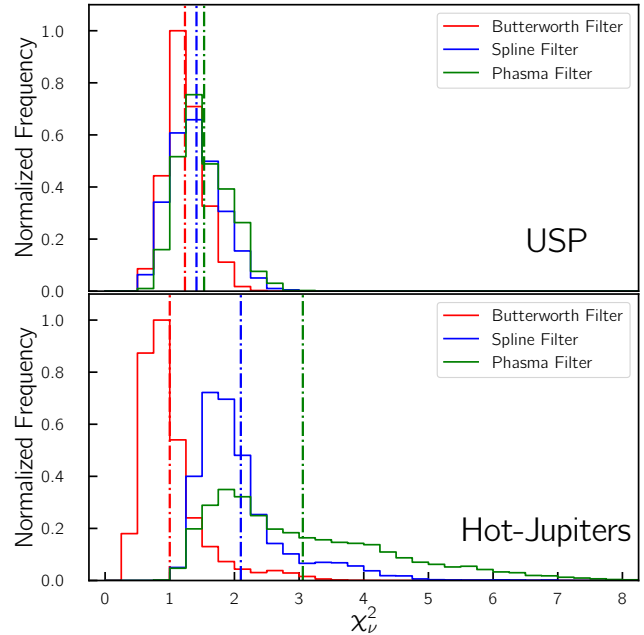


**Figure 5.** Top: Histogram of  $\chi^2_\nu$  for the retrieved signal of the ultra-short period planets (USP). The performance of all three flattening methods are similar. Bottom: Histogram of  $\chi^2_\nu$  for the retrieved signals observed for our samples of hot Jupiter targets. The mean value for shown with dotted lines  $\chi^2_\nu$  was 1.00 for Butterworth filters, 2.09 for Spline Filters, and 3.06 for Phasma Filters. Among the filtering techniques, we found the Butterworth filter statistically performed the best.

using detrended lightcurves of those system that did not show strong stellar modulations or unusual artifacts. Thus, there are inherent limitations to the tests we performed, and the performance of the filtering techniques is likely to change in the presence of complex red noise. We have also limited ourselves to three filtering techniques in this paper, but there are a host of techniques available which we did not fully explore. For instance, some authors have pointed out the possibility of using Gaussian Processes (Serrano et al. 2018) for disentangling the planetary phase curves amid strong stellar modulations induced by stellar rotation. However, given the computational cost, the complexity of the model along with the possibility of overfitting the phase curves dissuaded us from diving too deep into this technique (Millholland & Laughlin 2017). In the future, we plan to explore a wider suite of filtering, and data analysis techniques which might allow us to improve on the process we introduce here.

## 5. MODELS

For all the targets where we detect phase curves, we simultaneously fit for the primary transit, secondary eclipse and phase curve. We set the period as noted in the NASA exoplanet archive to produce phase folded light curves. The simultaneous fit of the transit and

the phase curves is primarily motivated to understand the cases with strong degeneracies among parameters as is the case of K2-31b. We initiate our MCMC model using the parameters reported in the discovery paper. For limb darkening, we use quadratic forms with uniform priors with range of 0.1 around the nearest values estimated by (Claret & Bloemen 2011). We similarly introduce priors in our MCMC for the scaled semi-major axis ( $a/R_*$ ) parameters to only accept values that yields the stellar density ( $\rho_*$ ) within  $5\sigma$  of spectroscopically derived stellar density (Winn 2010):

$$\rho_* + k^3 \rho_p = \frac{3\pi}{GP^2} \left( \frac{a}{R_*} \right)^3, \quad (11)$$

where  $G$  is Gravitational constant, and  $\rho_p$  is the planetary density. We ignore the contribution from  $k^3 \rho_p$  in our calculation. Additionally, we introduce a  $T_0$  offset parameter, which allows for an offset in the time of the conjunction. Note that the final reported value of  $T_0$  is calculated by appropriately combining this offset with the reported values in the original discovery paper.

We use the Mandel & Agol (2002) formalism as implemented in *batman* (Kreidberg 2015) in order to fit for the primary transit as well as the secondary eclipses. We supersample our light curve by a factor of 15, and set the exposure time to 29.4 minutes. For the phase curves, we used Bayesian Information Criteria (BIC) to choose the best model among three different models of phase curves: i) Thermal component with no significant nightside contribution (Model I) ii) Thermal component with significant nightside contribution (Model II) iii) Thermal component with a phase offset (Model III). In Model I, the secondary eclipse depth is constrained as a function of the amplitude of the reflective and thermal component, which can lead to compensated discovery of secondary eclipses. In Model II, the depth of the secondary eclipse is a free parameter without any priors. In Model III, we use the amplitude of the thermal component and phase offset as two free additional parameters compared to Model I. For all three models, we do not fit for phase variation during the transit, where we expect the transit to dominate the signal. We fit for a single mass parameter, which we refer to as the photometric mass ( $M_{Phot}$ ), to model both ellipsoidal variation as well as Doppler effects. For all of our models, we have used non-eccentric models motivated by the original discovery papers.

For exploring the parameter space, we used affine invariant MCMC implemented in *emcee* (Foreman-Mackey et al. 2013) running for 25,000 steps with 50 walkers. We use Gelman-Rubin statistics to ensure all of our MCMC converge. After the initial run, we compared the different models using Bayesian Information Crite-

rian (BIC), and re-ran the best model for 50,000 step by initializing our parameters around the best obtained values in the previous runs. We built the posterior distribution to estimate the error after removing the first 25,000 step of the data, and use the rest to estimate the error of the fit parameters. From posterior distribution, we report the median and  $1\sigma$  confidence interval corresponding to 15.8<sup>th</sup> percentile and 84.2<sup>th</sup> percentile respectively. For some parameters such as planetary mass or equilibrium temperature, we propagate the error from the stellar parameters with the errors we estimate from the posterior distribution in our final reported parameters.

For all our models we consider circular orbits and expect the secondary eclipse to occur exactly at the half phase. We ignore the Rømer delay, and the effects of eccentricity. These choices were motivated by the precision of the data as well as the reporting of no significant eccentricities in the discovery papers. As for the temperature of the planet, we report the dayside temperature by numerically solving the following equation:

$$\Delta = A_g \left( \frac{R_p/R_*}{a/R_*} \right)^2 + \left( \frac{R_p}{R_*} \right)^2 \frac{\int B(T_{Day})R(\lambda)d\lambda}{\int B(T_{eff})R(\lambda)d\lambda}, \quad (12)$$

where  $\Delta$  is the secondary eclipse depth,  $R_p/R_*$  is the scaled radius,  $a/R_*$  is the scaled semi-major axis, and  $B$  is Planck function which is convolved with the *Kepler* response function  $R(\lambda)$ . We solve Equation 12 for the geometric albedo ( $A_g$ ), and assume the day-side contribution is a function of the geometric albedo using aforementioned López-Morales & Seager (2007) formalism introduced in Equation 5. In order to report the dayside temperature, we set the re-radiation factor to 1/2 and assume  $A_B = 3/2A_g$  unless otherwise stated. Note this simple relation is not valid for planets in our solar system, and usually is likely to overestimate the value of the Bond Albedo (Dyudina et al. 2016). We also require the secondary eclipse depth to be strictly greater than or equal to the amplitude of the reflective and thermal component at phase 0.5. Similarly, the equilibrium temperature is calculated by setting the re-radiation factor to be 1/4.

## 6. RESULTS

### 6.1. Pre-Selected Targets

Prior to our study, three of K2 targets had reported phase curves: Qatar-2b (Dai et al. 2017b), K2-141b (Malavolta et al. 2018), and WASP-104b (Močnik et al. 2018). We re-run these objects through our pipeline, and fit the phase folded data and fit the phase curve models. For QATAR-2b, we obtained ellipsoidal variation amplitude of  $22.6^{+2.6}_{-2.5}$  ppm against  $15.4 \pm 4.8$  ppm, and Doppler modulation amplitude of  $10.8^{+1.3}_{-1.2}$  ppm against  $14.6 \pm 5.1$  ppm reported in Dai et al. (2017b).

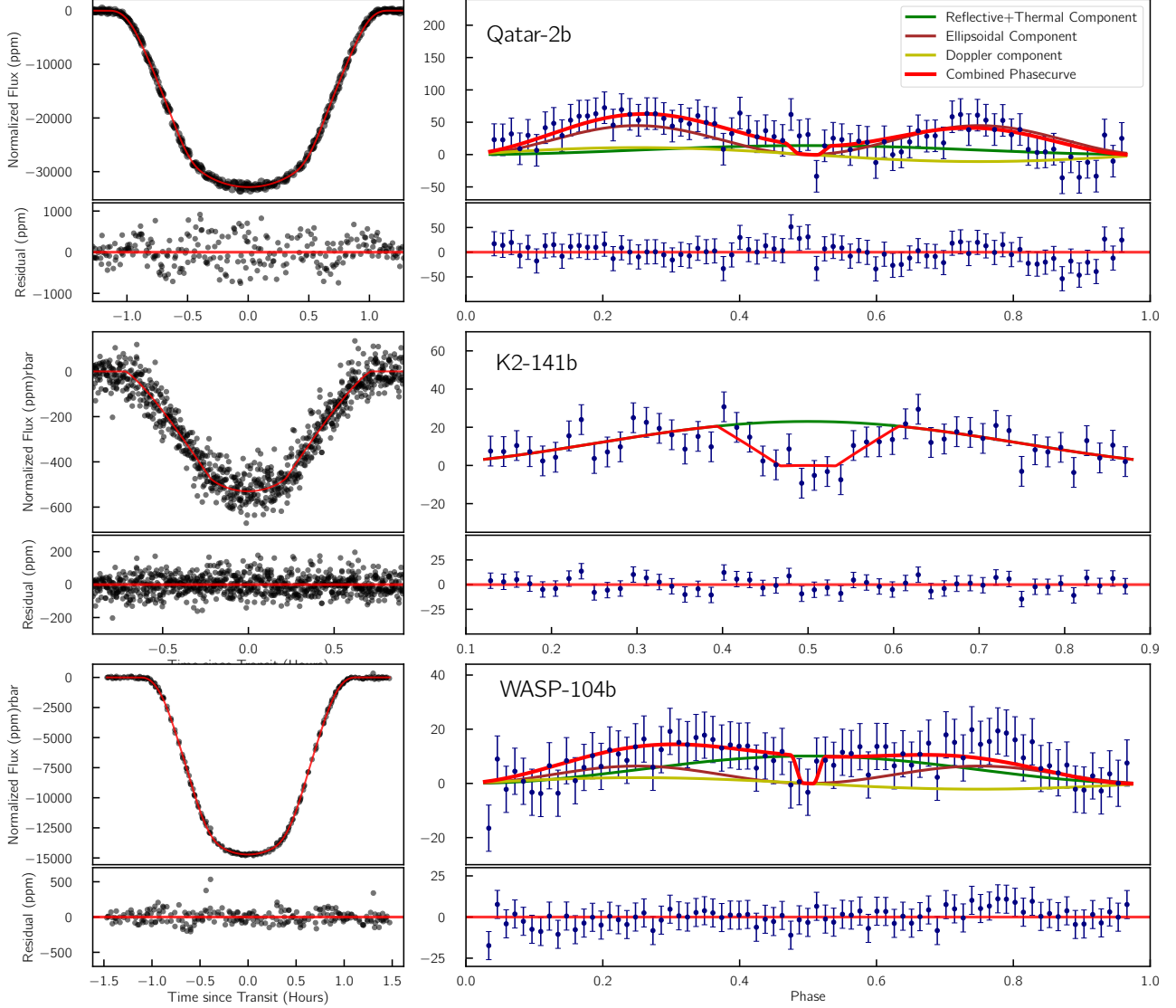


**Figure 6.** **Top:** Best fit of phase curve model for Qatar-2b using EVEREST data exhibiting strong ellipsoidal and Doppler variation. **Middle:** Best fit f phase curve model of K2-141b showing strong thermal and reflective modulation. **Bottom** Phase curve of WASP-104b observed in K2SFF detrended light curve exhibiting prominent ellipsoidal and Doppler effects. The fit parameters for all three targets are presented in Table 3.

This led to estimation of the photometric mass of  $3.27^{+0.40}_{-0.41} M_{\text{Jup}}$  consistent within  $2\sigma$  with the radial velocity mass of  $2.487 \pm 0.089 M_{\text{Jup}}$  (Bryan et al. 2012). The reflective and the thermal component in the phase curve constrain the geometric albedo with  $3\sigma$  confidence at 0.03 under the assumption  $A_g = 3/2A_B$ . For K2-141b, we use the same detrended lightcurve used in Malavolta et al. (2018), and the amplitude of the phase curve we find  $11.8 \pm 1.5$  ppm is consistent to their finding of occultation depth of  $23 \pm 4$  ppm. Under the assumption  $A_g = A_B$ , and numerically solving Equation 12, we estimate the geometric albedo of  $0.205^{+0.059}_{-0.077}$ . Similarly, we detect phase curve signal in

WASP-104b using K2SFF detrended light curve as had been reported in Moćnik et al. (2018). We find the reflective and thermal component at  $5.1 \pm 1.0$  against their reporting at  $4.8 \pm 2.1$  ppm, ellipsoidal variation amplitude at  $3.21 \pm 0.83$  against their reporting at  $6.9 \pm 2.2$  ppm, and Doppler effect amplitude at  $2.13 \pm 0.55$  against their reporting at  $4.2 \pm 1.9$  ppm. Also the photometric mass we obtain  $0.99 \pm 0.26 M_{\text{Jup}}$  is consistent within  $1.5\sigma$  with the radial velocity mass  $1.272 \pm 0.047$  (Smith et al. 2014).

Thus, our results for all three planets are largely consistent to the previous phase curves analyses. The fits using the best parameters for our targets are presented

in Figure 6, and the corresponding fit parameters are presented in Table 3. The light curves used in the anal-

ysis, as well as filtered light curves has been presented in the Appendix.

**Table 3.** Stellar and Planetary Parameters for Qatar-2b, K2-141b, and WASP-104b

Parameter	Unit	QATAR-2b	K2-141b	WASP-104b
<b>Stellar Parameters</b>				
$M_*$	$M_\odot$	$0.74 \pm 0.04^a$	$0.708 \pm 0.028^b$	$1.02 \pm 0.09^c$
$R_*$	$R_\odot$	$0.713 \pm 0.018^a$	$0.681 \pm 0.018^b$	$0.93 \pm 0.23^c$
$T_{eff}$	K	$4645 \pm 50^a$	$4599 \pm 79^b$	$5450 \pm 130^c$
[Fe/H]	dex	$-0.02 \pm 0.08^d$	$-0.06^{+0.08^b}_{-0.10}$	$-0.09 \pm 0.09^c$
$\log g_*$	cgs	$4.601 \pm 0.018^a$	$4.62^{+0.02^b}_{-0.03}$	$4.5 \pm 0.2^c$
$u$	-	$0.7165^e$	$0.7194^e$	$0.6459^e$
$g$	-	$0.5434^e$	$0.5452^e$	$0.4292^e$
<b>Pipeline</b>	-	<b>EVEREST</b>	<b>K2SFF<sup>b</sup></b>	<b>K2SFF</b>
<b>Orbital Parameters</b>				
Period	Days	$1.337116553 \pm 0.000000044^f$	$0.2803244 \pm 0.0000015^b$	$1.75540636 \pm 0.0000014^g$
$T_0 - 2450000$	BJD	$5617.5816109 \pm 0.0000087$	$7744.071542^{+0.000071}_{-0.000068}$	$7935.0702204 \pm 0.0000078$
$R_p/R_*$	-	$0.16526^{+0.00010}_{-0.00009}$	$0.02084^{+0.0005}_{-0.0002}$	$0.12041 \pm 0.00026$
$a/R_*$	-	$6.6769^{+0.006}_{-0.013}$	$2.30^{+0.05}_{-0.15}$	$6.732^{+0.041}_{-0.044}$
$b$	-	$0.036^{+0.038}_{-0.026}$	$0.23^{+(0.22)}_{-0.16}$	$0.7115^{+0.0063}_{-0.0059}$
Inclination	Deg	$89.69^{+0.22}_{-0.33}$	$84.2^{+4.1}_{-6.3}$	$83.933^{+0.087}_{-0.093}$
$e$	-	0 (assumed)	0 (assumed)	0 (assumed)
$\omega$	Deg	90 (assumed)	90 (assumed)	90 (assumed)
$u_1$	-	$0.5488^{+0.0016}_{-0.0008}$	$0.639^{+0.057}_{-0.051}$	$0.422^{+0.017}_{-0.015}$
$u_2$	-	$-0.0051^{+0.0043}_{-0.0020}$	$0.074^{+(0.073)}_{-0.061}$	$0.135^{+0.023}_{-0.015}$
<b>Phase Curve Parameters</b>				
$A_{Ref+Th}$	ppm	$6.9^{+3.1}_{-3.0}$	$11.8 \pm 1.5$	$5.1 \pm 1.0$
$A_{Ell}$	ppm	$22.6^{+2.6}_{-2.5}$	-	$3.21 \pm 0.83$
$A_{Dop}$	ppm	$10.8^{+1.3}_{-1.2}$	-	$2.13 \pm 0.55$
$T_{Day}$	K	$1711 \pm 24$	$2406^{+144}_{-76}$	$1698 \pm 24$
$T_{eq}$	K	$1434 \pm 20$	$1984^{+108}_{-59}$	$1422 \pm 20$
$A_g$	-	$< 0.03$ ( $3\sigma$ )	$0.205^{+0.059}_{-0.077}$	$0.0211 \pm 0.0068$
$M_{RV}$	$M_{Jup}$	$2.487 \pm 0.086^a$	$0.016 \pm 0.0013^b$	$1.272 \pm 0.047^c$
$M_{Phot}$	$M_{Jup}$	$3.27^{+0.40}_{-0.41}$	-	$0.99 \pm 0.26$

<sup>a</sup> Adopted from Bryan et al. (2012)

<sup>b</sup> Adopted from Malavolta et al. (2018)

<sup>c</sup> Adopted from Smith et al. (2014)

<sup>d</sup> Adopted from Maxted et al. (2015)

<sup>e</sup> Linear limb-darkening ( $u$ ) and gravity-darkening ( $g$ ) coefficients interpolated from Claret & Bloemen (2011)

<sup>f</sup> Adopted from Dai et al. (2017b)

<sup>g</sup> Adopted from Močnik et al. (2018)

## 6.2. New Discoveries

From the remaining 49 targets, we discovered phase curves among 6 of planets. Once discovered, we fitted

three standard models as discussed under §5. The unfiltered light curve, the outliers, as well as the filtered light curves from the process are added presented under

the Appendix. Below we present and discuss each of our targets in detail:

**Table 4.** Stellar and Planetary Parameters for K2-31b, HATS-9b, HATS-12b, and K2-107b

Parameter	Unit	K2-31b	HATS-9b	HATS-12b	K2-107b
<b>Stellar Parameters</b>					
$M_*$	$M_\odot$	$0.91 \pm 0.06^a$	$1.030 \pm 0.039^b$	$1.489 \pm 0.071^c$	$1.30 \pm 0.14^d$
$R_*$	$R_\odot$	$0.78 \pm 0.07^a$	$1.503^{+0.101b}_{-0.043}$	$2.21 \pm 0.21^c$	$1.78 \pm 0.16^d$
$T_{eff}$	K	$5280 \pm 70^a$	$5366 \pm 70^b$	$6408 \pm 75^c$	$6030 \pm 120^d$
[Fe/H]	dex	$0.08 \pm 0.05^a$	$0.340 \pm 0.050^b$	$-0.100 \pm 0.040^c$	$0.10 \pm 0.10^d$
$\log g_*$	cgs	$4.60 \pm 0.07^a$	$4.095 \pm 0.038^b$	$3.923 \pm 0.065^c$	$4.07 \pm 0.10^d$
$u$	-	$0.6554^e$	$0.5467^e$	$0.5317^e$	$0.5723^e$
$g$	-	$0.4611^e$	$0.3200^e$	$0.2751^e$	$0.3280^e$
<b>Pipeline</b>	-	EVEREST	K2SFF	K2SFF	EVEREST
<b>Orbital Parameters</b>					
Period	Days	$1.257850 \pm 0.000002^a$	$1.9153073 \pm 0.000005^b$	$3.142833 \pm 0.000011^c$	$3.31392 \pm 0.00002^d$
$T_0 - 2450000$	BJD	$2358.709367 \pm 0.000010$	$6124.258934^{+0.000032}_{-0.000033}$	$6798.955644 \pm 0.000075$	$6928.059202 \pm 0.000055$
$R_p/R_*$	-	$0.168^{+0.042}_{-0.023}$	$0.08414^{+0.00014}_{-0.00012}$	$0.06048^{+0.00056}_{-0.00042}$	$0.08335^{+0.00023}_{-0.00026}$
$a/R_*$	-	$5.66^{+0.10}_{-0.09}$	$4.556^{+0.011}_{-0.026}$	$5.47^{+0.19}_{-0.24}$	$5.890^{+0.082}_{-0.075}$
$b$	-	$1.022^{+0.053}_{-0.031}$	$0.065^{+0.065}_{-0.045}$	$0.29^{+0.12}_{-0.16}$	$0.7925^{+0.0074}_{-0.0082}$
Inclination	Deg	$79.61^{+0.51}_{-0.74}$	$89.29^{+0.55}_{-0.82}$	$87.0^{+1.8}_{-1.5}$	$82.27^{+0.18}_{-0.17}$
$e$	-	0 (assumed)	0 (assumed)	0 (assumed)	0 (assumed)
$\omega$	Deg	90 (assumed)	90 (assumed)	90 (assumed)	90 (assumed)
$u_1$	-	$0.560^{+0.029}_{-0.051}$	$0.5300^{+0.0072}_{-0.0049}$	$0.3227^{+0.0091}_{-0.0053}$	$0.437^{+0.027}_{-0.019}$
$u_2$	-	$0.261^{+0.039}_{-0.062}$	$-0.012^{+0.017}_{-0.016}$	$0.236^{+0.013}_{-0.006}$	$0.100^{+0.030}_{-0.021}$
<b>Phase Curve Parameters</b>					
$A_{Ref+Th}$	ppm	$12.27^{+0.85}_{-0.83}$	$11.6^{+2.3}_{-2.4}$	$7.5 \pm 1.9$	$12.8^{+1.9}_{-2.0}$
$A_{Ell}$	ppm	$17.07^{+0.77}_{-0.75}$	$14.7 \pm 2.3$	$10.2 \pm 1.8$	$11.6^{+1.8}_{-1.9}$
$A_{Dop}$	ppm	$5.55^{+0.33}_{-0.30}$	$2.08 \pm 0.33$	$2.53^{+0.54}_{-0.50}$	$3.03^{+0.51}_{-0.50}$
$T_{Day}$	K	$1860 \pm 35$	$2100 \pm 29$	$2240^{+82}_{-68}$	$2005^{+26}_{-27}$
$T_{eq}$	K	$1554 \pm 29$	$1751 \pm 24$	$1849^{+61}_{-52}$	$1669^{+20}_{-21}$
$A_g$	-	$< 0.047 (3\sigma)$	$0.027^{+0.015}_{-0.017}$	$0.07 \pm 0.04$	$0.102 \pm 0.023$
$M_{RV}$	$M_{Jup}$	$1.774 \pm 0.079^a$	$0.837 \pm 0.029^b$	$2.38 \pm 0.11^c$	$0.84 \pm 0.08^d$
$M_{Phot}$	$M_{Jup}$	$2.09 \pm 0.18$	$0.98 \pm 0.16$	$2.13^{+0.46}_{-0.43}$	$1.57^{+0.26}_{-0.27}$

<sup>a</sup>Adopted from Grziwa et al. (2016)

<sup>b</sup>Adopted from Brahm et al. (2015)

<sup>c</sup>Adopted from Rabus et al. (2016)

<sup>d</sup>Adopted from Eigmüller et al. (2017)

<sup>e</sup>Linear limb-darkening ( $u$ ) and gravity-darkening ( $g$ ) coefficients interpolated from Claret & Bloemen (2011)

### 6.2.1. K2-31b

Given the short period, high mass and large scaled radius, K2-31b was the best candidate among K2 dis-

covered planets to have a detectable phase curve. Our analysis of the data indeed shows the presence of a robust phase curve with all of the components present.

K2-31b is a grazing hot Jupiter with mass of  $\sim 1.8 M_{\text{Jup}}$  discovered by [Grziwa et al. \(2016\)](#). Due to the grazing nature of the transit, which introduces a degeneracy between scaled radius and inclination, the radius of the planet has not very precisely determined. Our MCMC yielded the scaled radius of the planet of  $0.168_{-0.023}^{+0.042}$ , which assuming a host star of radius  $0.78 R_{\odot}$  translates into physical radius of  $1.28_{-0.17}^{+0.32} R_{\text{Jup}}$ .

For our analysis, we use the EVEREST detrended light curve and obtain a photometric mass ( $M_{\text{phot}}$ ) of  $2.09 \pm 0.18 M_{\text{Jup}}$  consistent within  $2\sigma$  to the RV-based mass ( $M_{\text{RV}}$ ) of  $1.774 \pm 0.079 M_{\text{Jup}}$  reported in the discovery paper. [Grziwa et al. \(2016\)](#) points out that due to its grazing nature which is often interpreted as eclipsing binaries, planets like K2-31b are usually neglected for RV follow-up. We show here that a target’s planetary nature can be revealed by estimating mass through the optical phase curve. In the discovery paper, [Grziwa et al. \(2016\)](#) constrains the upper limit on the geometric albedo of K2-31b at 0.40, due to the absence of any visible secondary eclipse. By fitting for the whole phase curve, we are able to constrain the geometric albedo to 0.047 at  $3\sigma$  confidence, a dark planet even by the standard of hot Jupiters ([Esteves et al. 2015](#); [Angerhausen et al. 2015](#)). Yet, the grazing nature of the transit leads to strong degeneracy among parameters (see [Figure 7](#)), as well as the underlying assumptions for the thermal emission and the Bond albedo leaves room for unaccounted systematic errors for such estimation. The degeneracy among different parameters, however is not as strong for the observed photometric mass. A ringing feature appears to present in the residual, although it is not a very prominent one.

### 6.2.2. HATS-9

HATS-9b is a hot Jupiter that was discovered in the Campaign 7 *K2* field ([Brahm et al. 2015](#)). [Bayliss et al. \(2018\)](#) updated the system parameters using the *K2* lightcurve, however did not report the phase curve. We use K2SFF detrended light curve for this particular analysis given its precision, and in examining the light curve for the potential phase curve, we detect the ellipsoidal variation for HATS-9b which yielded a photometric mass of  $0.98 \pm 0.16 M_{\text{Jup}}$  consistent within  $1\sigma$  to the reported RV mass of  $0.837 \pm 0.029 M_{\text{Jup}}$ . Fitting for the reflective and the thermal component of the phase curve yielded the geometric albedo of  $0.027_{-0.017}^{+0.015}$ . The fit using the best parameters is shown in [Figure 8](#), and the corresponding parameters are reported in [Table 4](#). Ringing effects appears to be more prominent among the residual of HATS-9b.

### 6.2.3. HATS-12b

HATS-12b ([Rabus et al. 2016](#)) was another hot Jupiter discovered in the *K2* Campaign 7 field. An abrupt jump in the data was observed in both detrended light curves around BJD - 2457333.1 (see [Figure 3](#)), possibly due to a change in the pixel responsivity ([Jenkins et al. 2010](#)). We use K2SFF detrended light curves for the analysis, and corrected for the jump by using a linear regression at the break point. Marked as one of the promising targets using our SNR metric, we see distinct phase curve emerge in the phase folded light curve. The phase curves exhibits particularly prominent ellipsoidal variation, fitting for which leads to a mass of  $2.13_{-0.43}^{+0.46} M_{\text{Jup}}$  consistent within  $1\sigma$  to the reported RV mass of  $2.38 \pm 0.11 M_{\text{Jup}}$  ([Rabus et al. 2016](#)). The good agreement comes with a little surprise given HATS-12 has a stellar mass of  $1.489 \pm 0.071 M_{\odot}$ , which lies above  $1.4 M_{\odot}$ , a threshold beyond which the tidal-equilibrium approximation assumed for calculating the ellipsoidal variation amplitude may not strictly hold ([Pfahl et al. 2008](#)). We find the geometric albedo is  $0.07 \pm 0.04$ , typical for hot Jupiters. The fit using the best set of parameters is shown in [Figure 9](#), and the corresponding parameters are reported in [Table 4](#). Note the secondary eclipse primarily comes as a constraint from the use of Model I, which is favored among three models using BIC.

### 6.2.4. K2-107b

K2-107b was reported in [Eigmüller et al. \(2017\)](#) where using high-resolution imaging, a few nearby companions were detected. However, the dilution due to these companions is only  $0.5 \pm 0.1\%$  of the *K2* aperture flux and therefore was ignored in this analysis. A few nearby companions were detected with high resolution imaging, which are positioned in the *K2* aperture, however the combined dilution factor correction due to these companion is  $0.005 \pm 0.001$ , therefore negligible for the calculation we are considering. We use the EVEREST detrended light curve for the fitting purposes, which yields a photometric mass of  $1.57_{-0.27}^{+0.26} M_{\text{Jup}}$ , which is within  $3\sigma$  of RV mass reported at  $0.84 \pm 0.08 M_{\text{Jup}}$ . The estimated geometric albedo is  $0.102 \pm 0.023$ . The fit of K2-107b is shown in [Figure 9](#), and the parameters are reported in [Table 4](#). Some structural features are present in the residuals potentially because of the ringing effects from filtering process. Like in HATS-12b, the secondary eclipse is a constraint from the use of Model I. The larger scatter of the data points during the secondary eclipse potentially results from the masking of these points during the filtering process.

### 6.2.5. K2-131b

K2-131b is an ultra-short period planet with a period of 0.3693 days reported in [Dai et al. \(2017a\)](#). For this work, we use the light curve from EVEREST pipeline,

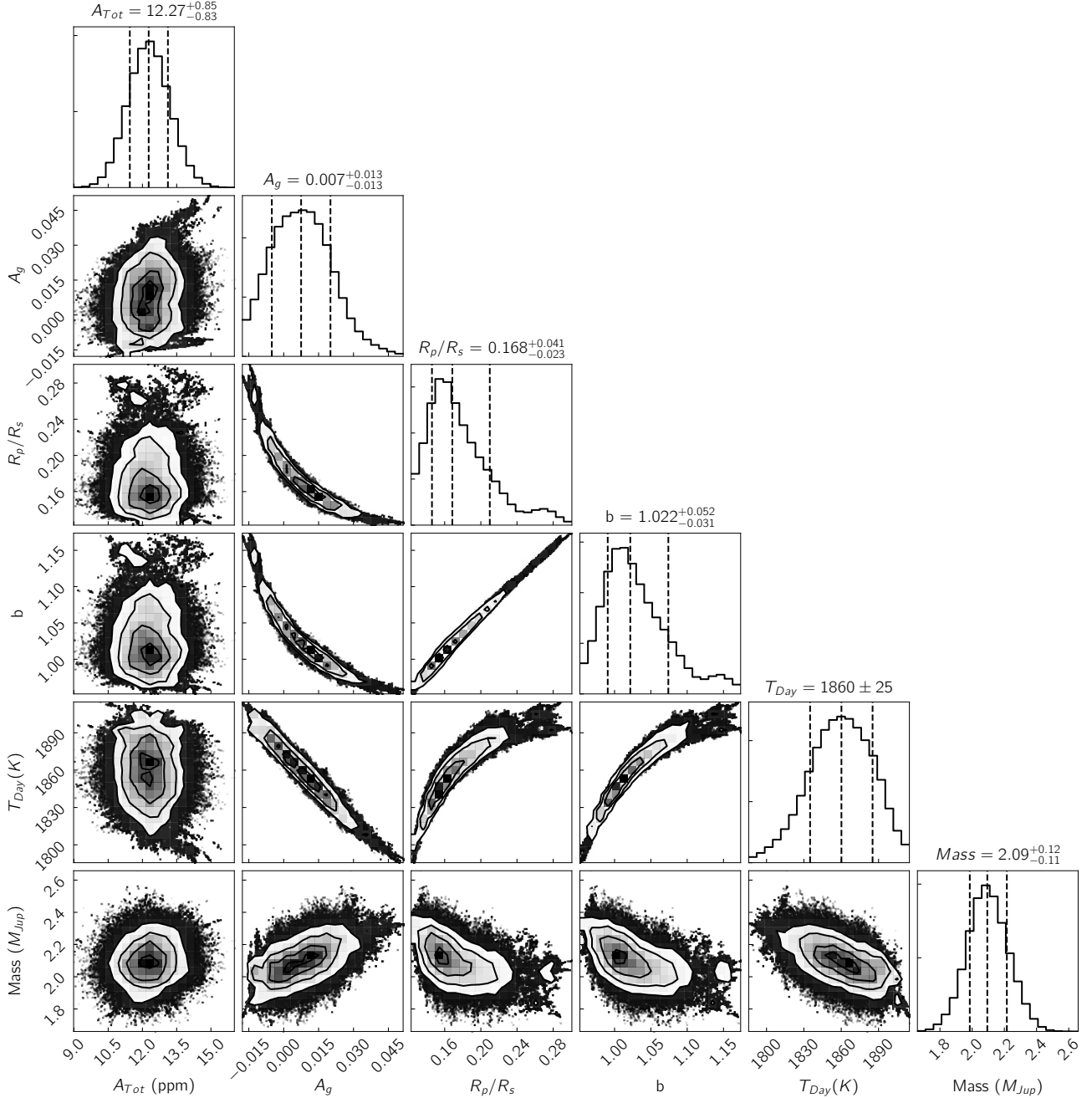


**Figure 7.** Corner plot showing the posterior distribution and co-variance among different fit parameters of K2-31b. A strong degeneracy is present among the scaled radius ( $R_p/R_*$ ), geometric albedo ( $A_g$ ), impact parameter ( $b$ ), and day-side temperature ( $T_{Day}$ ), while the mass of the planet exhibits minimal correlation with most of the parameters. The errors from the stellar parameters have not been propagated.

and only from the second half of Campaign 10 as the first half of the data shows strong systematic effects. In the phase folded data, we detect the secondary eclipse at  $25.4 \pm 8.2$  ppm. We only fit for reflective and thermal component, as the ellipsoidal and Doppler beaming signal from the small planets is not detectable. Unlike for the hot Jupiters in our lists, we use an altered relation between the geometric albedo and Bond Albedo as  $A_B = A_g$ . The modified relation allows for values

greater than 0.66 for geometrical albedo, and such deviation from the traditional Lambertian relation ( $A_B = \frac{3}{2}A_g$ ) is expected as it tends to overestimate the Bond Albedo (Dyudina et al. 2016). The fits showing the best obtained parameters are shown in Figure 10, and the parameters are reported in Table 5. Note the geometric albedo of  $0.27^{+0.31}_{-0.27}$  was estimated for K2-131b.

### 6.2.6. K2-106b

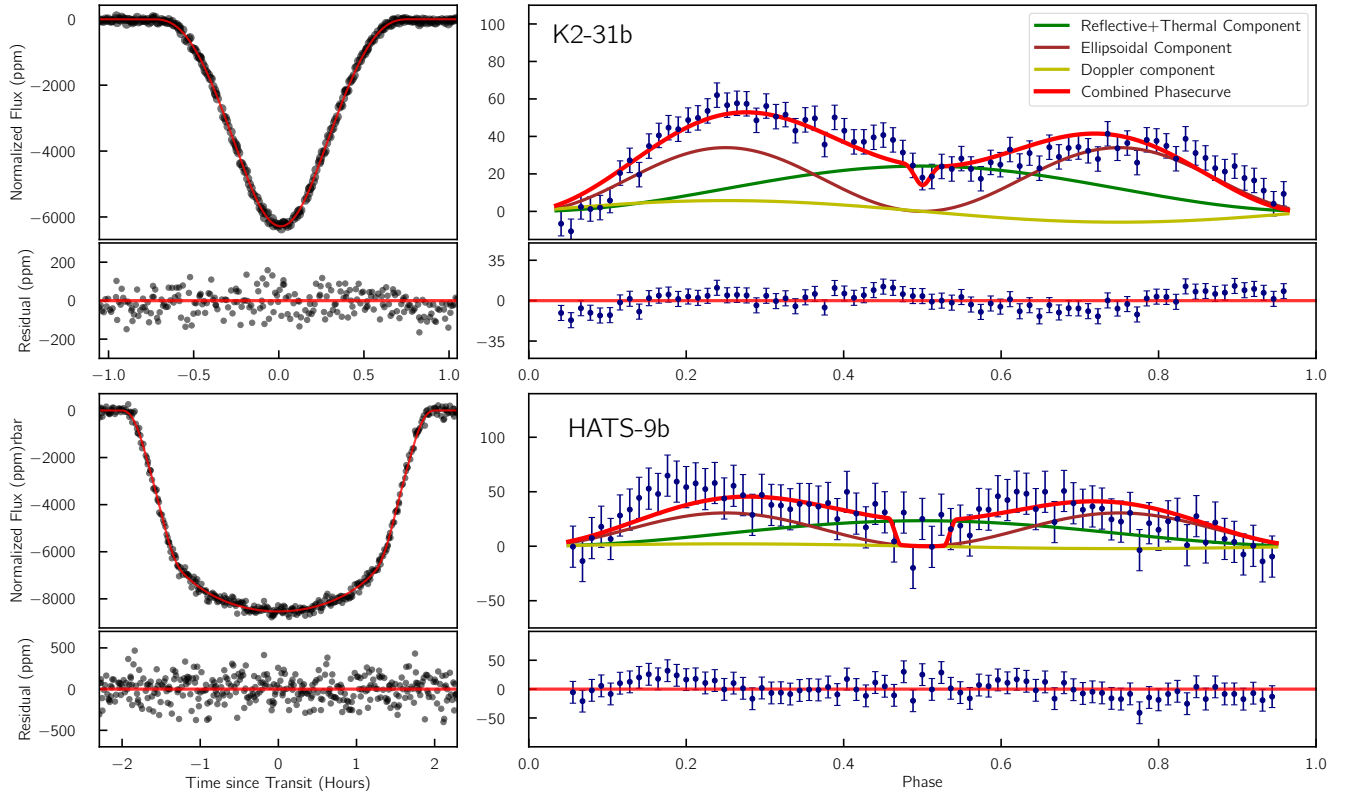


**Figure 8.** Upper-left: Transit fit using the best fit parameter for K2-31b and the residual. Upper-right: Phase curve signal using the best obtained parameter for K2-31b with different components. The data was binned to have a total number of bins of 75, thus each bin size corresponds to 0.37 hours. Lower-left: Transit fit using the best fit parameter for HATS-12b and the residual. Lower-right: Phase curve signal using the best set of visualization in HATS-9b with different components and its residual. The data was binned to have a total number of bins of 75, thus each bin size corresponds to 0.55 hours.

K2-106 is a multi-planetary system with an ultra short period planet with period of 0.57133 days. It was first identified as a candidate in Adams et al. (2017), and subsequent RV campaigns verified the planetary nature of the signal with mass reported in Guenther et al. (2017) and Simukoff et al. (2017). For our analysis, we adopted the values from the latter. We detect the secondary eclipse at  $23.5^{+4.9}_{-5.1}$  ppm. Reflective and thermal component constitute the dominant part of the phase curve (see Figure 10), and like K2-131b, we do not fit for either ellipsoidal variation or Doppler beaming due to negligible expected contributions. In order to estimate the temperature, we similarly use the modified relation i.e.  $A_B = A_g$ , which yielded a geometric albedo of  $0.62^{+0.22}_{-0.34}$ . The fit itself is shown in Figure 10, and the corresponding fit parameters are reported in Table 5.

## 7. SECONDARY ECLIPSE

To our knowledge, K2-260b is the only planet up until now with a robust secondary eclipse detection among the planets discovered by *K2* (Johnson et al. 2018). Since secondary eclipses characterize the geometric albedo as well as the temperature contrast just through observation of the depth of secondary eclipse alone, it is less

prone to periodic or quasi-periodic noises. We therefore uniformly look for secondary eclipse signals for all planets reported in Table 1.

For our secondary eclipse detection pipeline, we masked the range of data at transit as well as the phase of 0.5, where we estimate the secondary eclipse to occur. To the rest, we fitted a third degree polynomial with a length of 0.75 days and phase folded the data to build up the signal. The rest of the pipeline includes the same iterative outliers detection technique as was implemented for the phase curves. In this fashion, we detected secondary eclipse in K2SFF light curves of HATS-11b at  $62 \pm 12$  ppm (see Figure 11). We use the depth to solve for the dayside temperature as well as the albedo for HATS-11b. The fit parameters are reported in Table 5.

The detection of a secondary eclipse without the phase curve, as is the case for HATS-11b, raises an interesting question - why is there a secondary eclipse without a phase curve? HATS-11b has an easy-to-model stellar continuum that makes extracting a phase curve rather easy, although the signal may have been distorted during one of the many data processing steps. It also could be that the source of phase curve is predominantly thermal,

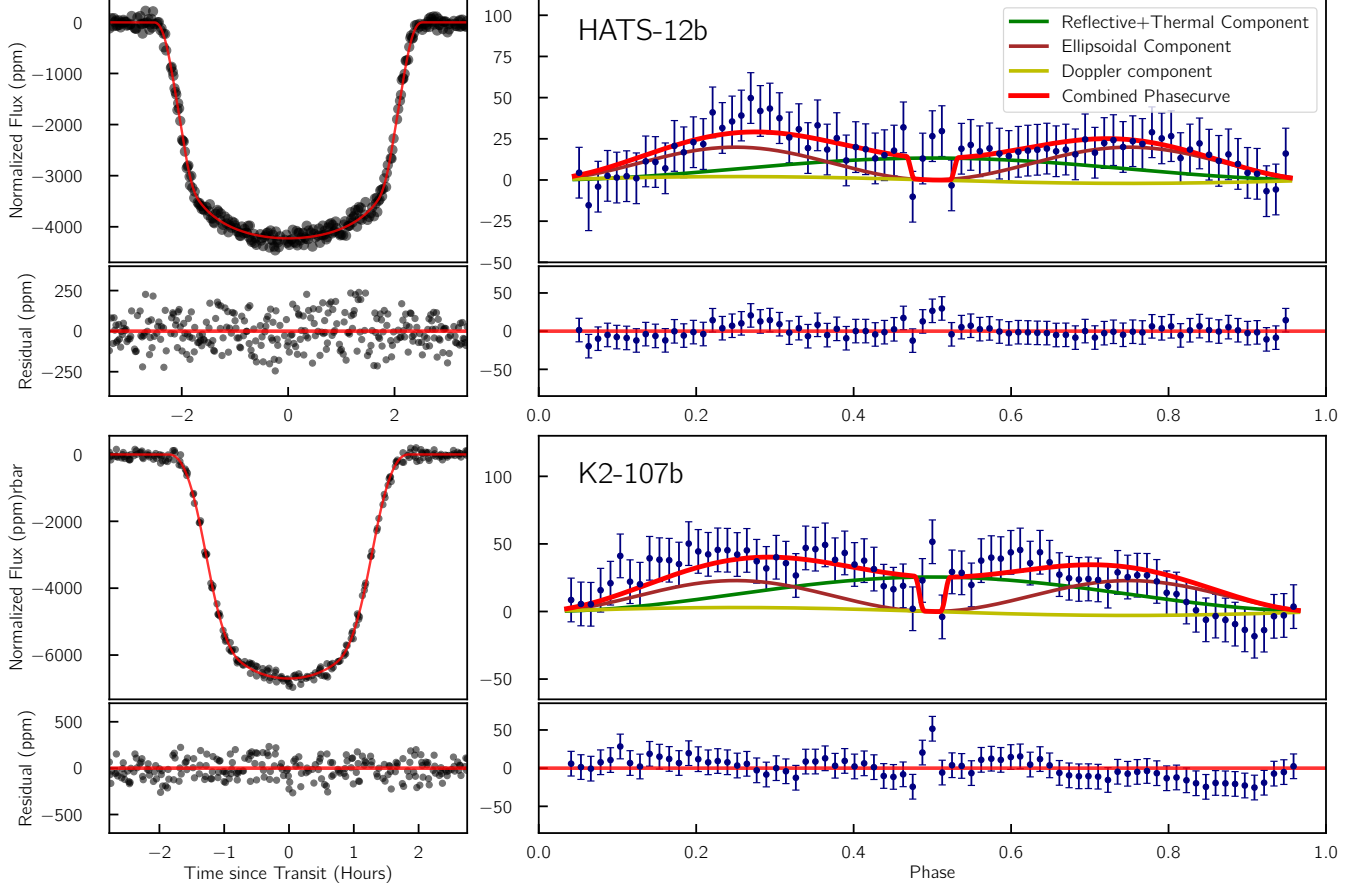


**Figure 9.** Upper-left: Transit fit using the best fit parameter for HATS-12b and its residual. Upper-right: Phase curve signal using the best obtained parameter for HATS-12b with different components. The data was binned to have a total number of bins of 75, thus each bin size corresponded to 0.91 hours. Lower-left: Transit fit using the best fit parameter obtained for K2-107b and its residual. Lower-right: Phase curve signal using the best set of visualization in K2-107b with different components and its residual. The data was binned to to have a total number of bins of 75, thus each bin size corresponds to 0.99 hours.

and an efficient heat transportation between day and night-side significantly weakens the phase curve signal. Another explanation could be that the planetary atmosphere at the depth the phase curve probes is rotating at a pseudo-synchronous rate (Adams & Laughlin 2018) washing out the signal as we phase fold the light curve. Note using EVEREST light curve for HATS-11b, which has comparable precision level as the K2SFF light curve, the secondary eclipse depth was detected at the level of  $36 \pm 11$  ppm, still a  $3\sigma$  detection. It still lacks a robust phase curve.

## 8. NON-DETECTION

For the most part, our formulated metric is expected to perform as well as, if not better than, the previously used metrics such as  $a/R_* < 10$  in Esteves et al. (2013), and  $R_p > 4R_\oplus$ ,  $P < 10$  days and  $V_{\text{mag}} < 15$  in Angerhausen et al. (2015). However, our precision approximation relation deviates from the actual observed value for fainter stars, which in the future could be improved by using the empirically obtained noise floor. Similarly

our calculation of SNR ratio could underestimate the signal for small period planets due to potentially non-negligible contribution from tidal heating of the planets.

The presence of strong stellar activity can make the process of disentangling the phase curve difficult. The degree of difficulty particularly depends on the separation of the frequency and its harmonics of stellar modulation signals from the phase curve signal’s frequencies. For instance, for targets for which phase curve signal was successfully extracted such as K2-31b, there is little overlap between power from stellar rotation and phase curve (see Figure 12). On the other hand, for targets such as WASP-85Ab, K2-29b and K2-100b, the presence of prominent stellar activity dominates the frequency spectrum, thereby making the process of phase curve extraction difficult. For other targets such as WASP-118b and HATS-P-56b, the presence of stellar pulsation potentially induced by the planet similarly makes the disentangling process difficult (Huang et al. 2015; Moćnik et al. 2017). A clear sign of stellar pulsation has been

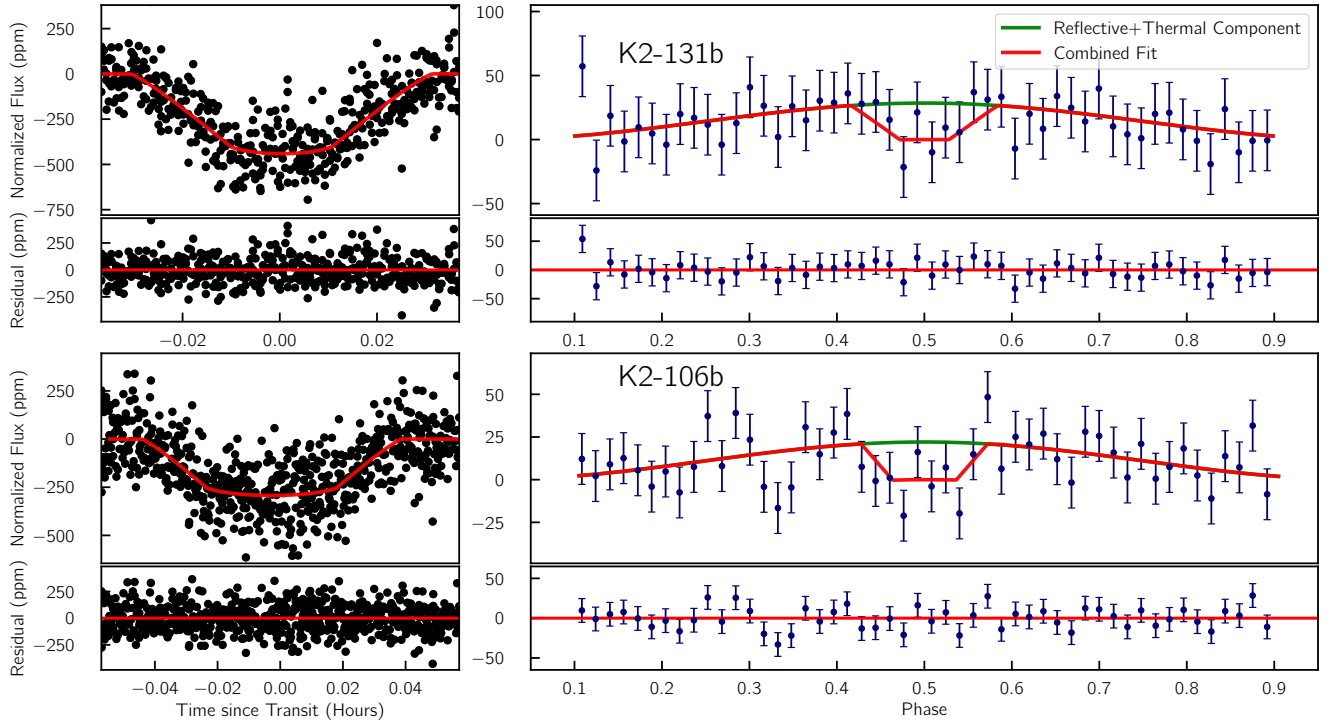


**Figure 10.** Upper-right: Transit fit using the best parameter for K2-131b. Upper-left: Phase curve modulation showing reflective and thermal component in K2-131b with a secondary eclipse depth at  $25.4 \pm 8.2$  ppm. A total of 50 bins are used which corresponds to bin size of 0.14 hours. Lower-right: Transit fit using the best parameter for K2-106b. Lower-left: Phase curve modulation showing reflection and thermal component modulation in the folded light curve of K2-106b with a secondary eclipse depth at  $23.5^{+4.9}_{-5.1}$  ppm. A total of 50 bins are used which corresponds to bin size of 0.22 hours.

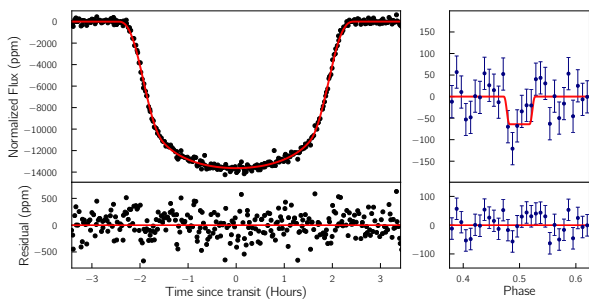


**Figure 11.** Transit fit (left) is shown for HATS-11b using best fit parameters which are reported in Table 5. The secondary eclipse (right) is detected at  $62 \pm 12$  ppm.

observed in similar spectral type but highly eccentric system – HAT-P-2b (de Wit et al. 2017).

As for cases such as K2-137b, which has a large estimated ellipsoidal variation, no phase curve was detected because the mass was the upper limit reported in the discovery paper, leading to over-estimation of the signal (Smith et al. 2018). Similarly, for targets such as K2-22b, a disintegrating planetary system (Sanchis-Ojeda et al. 2015), the assumptions of our model does not hold. As for some of the targets such as WASP-47 system, we detect phase curve for the inner most planet at a significance level of  $2\sigma$ , which we have not reported in this

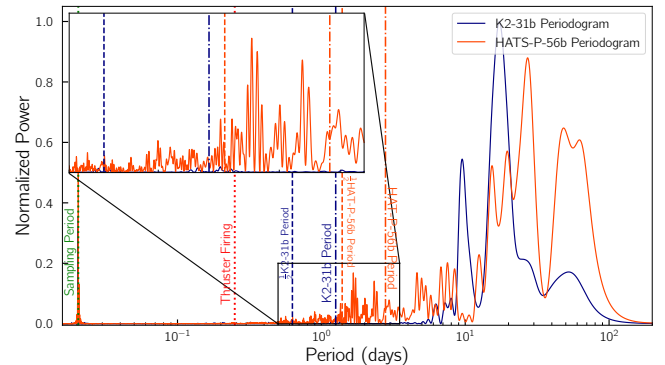


**Figure 12.** Lomb-Scargle Periodogram of the time series of K2-31b and HAT-P-56b after removal of outliers and transit points. Note the presence of significant power of HAT-P-56 near and around the planetary period while such signal is absent in case of K2-31b. The power at 6 hours (thruster firing) exhibits minimal power in both of the targets.

paper.

## 9. DISCUSSION

### 9.1. Model Performance

The photometric mass for the four hot Jupiters, while less precise than their RV counterparts, are consistent at  $3\sigma$  level with each other in all of the six cases. Hence, the model we use appear to be well-calibrated. In fact,

the model has been tested for a wide range of masses – planetary to stellar mass, although there are some cases of where discrepancy between the model and the data do exist (Faigler & Mazeh 2015b; Eigmüller et al. 2018). Such inconsistencies in the photometric mass in the case of hot Jupiters can arise due to the thermal component with a phase-shift resulting from super-rotation (Faigler et al. 2015a). When we independently fit for ellipsoidal variation and Doppler boosting, the mass ranges derived from the Doppler effect were not as consistent with the RV mass as the one obtained from the ellipsoidal variation. For instance, the median of the distribution of ellipsoidal mass in all cases i.e. for Qatar-2b, WASP-104b, K2-31b, HATS-9b, and K2-107b was off compared to Doppler mass. While such discrepancies could arise because of the fact that Doppler effects are often times too smaller compared to their ellipsoidal counterpart, and at the same time they are affected from the contribution of phase shifted thermal component or asymmetries in the reflective component. We refrained from using more complex models given the precision of data did not support such choices.

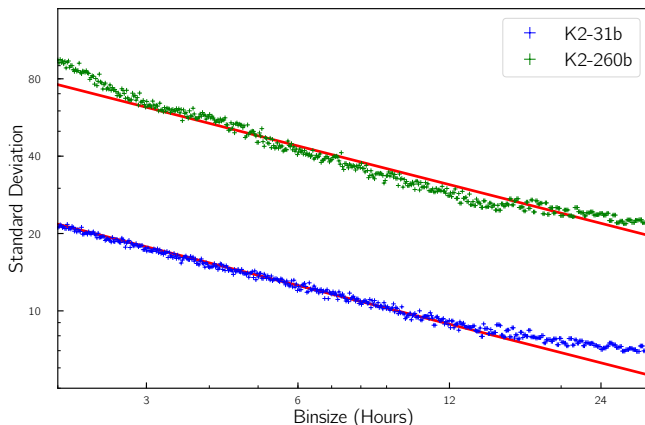


**Figure 13.** Observed RMS vs the bin size in the residual obtained by fitting phase curve models in K2-260b and K2-31b. Binning in K2-31b follows the expected power law of 0.5, whereas for K2-260b strongly deviates from it. The red lines are idealized cases drawn for both data sets.

### 9.2. Signal Fidelity

*K2* has been used for used in studies related to asteroseismology (Lund et al. 2016), white dwarfs pulsation (Hermes et al. 2017), AGN variability (Aranzana et al. 2018), and stellar rotation (Angus et al. 2016; Esselstein et al. 2018). These studies have shown that *K2* pipeline can retain astrophysical variability signals if the period under consideration is less than 15 days (Van Cleve et al. 2016). As all of our targets have precisely known periods which fall well under 15 days, we can confidently extract the relevant signal. The major trouble in phase curve

extraction instead is restricted by other dominant forms of accompanying stellar variation.

There are additional tests we perform to test the fidelity of the signal. For instance, K2-260b is close to spin-orbit resonance. Despite reporting a prominent secondary eclipse, Johnson et al. (2018) did not report the phase curve for the planet. We ran our pipeline, and fitted the phase folded light curve, which however yielded a mass inconsistent with reported RV value by more than  $3\sigma$ . The residuals from the fit show the correlated noise which stand out in RMS vs bin size plots compared to the residuals from the targets such as K2-31b for which the phase curve is reported (see Figure 13). All of our phase curve targets have residuals that closely follow the expected the power law.

### 9.3. Ultra-Short Period Planet

With our discovery, K2-131b and K2-106b now join the group of other ultra-short planets such as Kepler-78 (Sanchis-Ojeda et al. 2013), Kepler-10b (Esteves et al. 2013), 55-Cnc-e (Demory et al. 2016) and K2-141b (Malavolta et al. 2018) with a detected secondary eclipse. Note all of these planets are rocky super-Earths with high densities and high geometric albedos possibly due to the presence of refractory surfaces. We used the modified relation  $A_g = A_B$  to estimate the geometric albedo for all of the super-Earth targets to allow geometric values greater than 0.66. Additionally, we suspect that there might be non-negligible additional source of heating such as tidal heating present in these systems which scales strongly with distance from the host star ( $a$ ) and eccentricity ( $e$ ) as follows:

$$H = \frac{63}{4} \frac{(GM_*)^{3/2} M_* R_p^5}{Q_p} a^{-15/2} e^2 \quad (13)$$

where  $H$  is the tidal heating rate,  $M_*$  is the stellar mass,  $R_p$  is the planetary radius, and  $Q_p$  is the tidal dissipation parameter (Jackson et al. 2008). The fact that most of these planets are multi-planetary system suggest mechanisms similar to Io as a Galilean moon of Jupiter may also be acting on these planets (Peale et al. 1979; Demory et al. 2016). While tidal heating will increase the overall equilibrium temperature of these planets, thereby increasing the nightside contribution, the precision of *K2* data does not allow us to explore such effects. Yet, asymmetries between the day and nightside can still occur due to mechanisms such as volcanism (Gelman et al. 2011), which would also contribute to the phase curve signals.

### 9.4. Spectroscopic Follow-Up

Phase curves can be used to infer the existence of atmospheres for the close-in hot planets through the detection of the offset of the phase curve peaks (Shporer

& Hu 2015; Demory et al. 2016; Angelo & Hu 2017). Similarly, the geometric albedo can be linked to atmospheric processes such as clouds, which are known to play important roles in the transmission spectrum (Kreidberg et al. 2014; Sing et al. 2016). Currently, there are only a few targets with reported geometric albedo

which have been followed up with spectroscopic observation. However, this will drastically change as *TESS* discovers a large sample of optimal targets. This could enable screening out the best planetary candidates for the follow-up atmospheric studies using the geometric albedo as a guideline.

**Table 5.** Stellar and Planetary Parameters for K2-131b, K2-106b, and HATS-11b

Parameter	Unit	K2-131b	K2-106b	HATS-11b
<b>Orbital Parameters</b>				
$M_*$	$M_\odot$	$0.84 \pm 0.03^a$	$0.92 \pm 0.03^b$	$1.000 \pm 0.060^c$
$R_*$	$R_\odot$	$0.81 \pm 0.03^a$	$0.95 \pm 0.05^b$	$1.444 \pm 0.057^c$
$T_{eff}$	K	$5200 \pm 100^a$	$5496 \pm 46^b$	$6060 \pm 150^c$
[Fe/H]	dex	$-0.02 \pm 0.08^a$	$0.06 \pm 0.03^b$	$-0.390 \pm 0.060^c$
$\log g_*$	cgs	$4.62 \pm 0.10^a$	$4.42 \pm 0.05^b$	$4.118 \pm 0.026^c$
u	-	$0.6604^d$	$0.6294^d$	$0.5467^d$
g	-	$0.4737^d$	$0.4181^d$	$0.3199^d$
<b>Pipeline</b>	-	<b>EVEREST</b>	<b>K2SFF</b>	<b>K2SFF</b>
<b>Orbital Parameters</b>				
Period(Days)	Days	$0.3693038 \pm 0.0000091^a$	$0.571336 \pm 0.000020^b$	$3.6191613 \pm 0.0000099^c$
$T_0 - 2450000$	BJD	$7582.93620^{+0.00031}_{-0.00033}$	$6226.43381^{+0.00040}_{-0.00039}$	$6574.96536^{+0.00017}_{-0.00016}$
$R_p/R_*$	-	$0.01968^{+0.0016}_{-0.0006}$	$0.01584^{+0.00086}_{-0.00036}$	$0.10707 \pm 0.00013$
$a/R_*$	-	$2.61^{+0.23}_{-0.58}$	$2.73^{+0.16}_{-0.47}$	$7.006^{+0.010}_{-0.015}$
e	-	0 (fixed)	0 (fixed)	0 (fixed)
$\omega$	-	90 (fixed)	90 (fixed)	0 (fixed)
b	-	$0.43^{+0.32}_{-0.31}$	$0.37^{+0.31}_{-0.25}$	$0.036^{+0.039}_{-0.025}$
Inc	Deg	$80.5^{+7.0}_{-12.4}$	$82.3^{+5.4}_{-9.7}$	$89.70^{+0.21}_{-0.32}$
$u_1$	-	$0.511^{+0.077}_{-0.054}$	$0.451^{+0.072}_{-0.063}$	$0.383^{+0.007}_{-0.008}$
$u_2$	-	$0.141^{+0.077}_{-0.056}$	$0.228^{+0.068}_{-0.068}$	$0.2000^{+0.0087}_{-0.0039}$
<b>Secondary Eclipse Fit Parameters</b>				
$A_{Ref+Th}$	ppm	$12.7 \pm 4.2$	$11.7 \pm 2.5$	-
$\Delta$	ppm	$25.4 \pm 8.2$	$23.5^{+4.9}_{-5.1}$	$62 \pm 12$
$A_g$	-	$0.27^{+0.31}_{-0.27}$	$0.62^{+0.22}_{-0.34}$	$0.249^{+0.057}_{-0.058}$
$T_{Day}$	K	$2300^{+740}_{-425}$	$2200^{+630}_{-470}$	$1704^{+54}_{-60}$
$T_{Eq}$	K	$2010^{+450}_{-270}$	$1800^{+470}_{-375}$	$1428^{+44}_{-49}$

<sup>a</sup>Adopted from Dai et al. (2017a)

<sup>b</sup>Adopted from Sinukoff et al. (2017)

<sup>c</sup>Adopted from Rabus et al. (2016)

<sup>d</sup>Interpolated from Claret & Bloemen (2011)

### 9.5. Future Prospects

With the launch of *TESS* and the up-coming future missions like CHaracterising ExOPlanet Satellite (*CHEOPS*; Broeg et al. 2013) James Webb Space

Telescope (*JWST*; Beichman et al. 2014), PLAnetary Transits and Oscillation of stars (*PLATO*; Rauer et al. 2014), and Atmospheric Remote-sensing Exoplanet Large-survey (*ARIEL*; Tinetti et al. 2016), there will be plentiful opportunities in the future for phase-curves

studies. In fact, the phase curve of WASP-18b has already been reported in Sector 2 *TESS* data (Shporer et al. 2018), and more will definitely be detected over the course of the mission. These studies will allow an unprecedented opportunity to learn about exoplanet atmospheres, while allowing us to refine our models with more precise data, and potentially disentangle the often degenerate reflective and the thermal components (Placek et al. 2016).

## 10. CONCLUSION

We have significantly increased the number of phase curves discovered by *K2* with four hot Jupiters' phase curves that yield photometric masses within  $3\sigma$  of the reported RV-based masses, and two additional short period super-Earths with  $3\sigma$  level secondary eclipse detections along with corresponding phase curves. The availability of the precise light curves as well as the use of a more aggressive filtering procedure tested with signal injection facilitated in our venture. The consistency of the obtained mass, although for a small but non-negligible number of planets, raises the possibility of developing a tool for preliminary planetary signal validation for *TESS* candidates. As we stand on the cusp of discovering many more planets, and will re-observe many of the hot Jupiters, an opportunity will be presented to refine our phase curve models, build a larger sample of planets with detected phase curves and open up novel lines of inquiry. Such possibilities and others

should strongly motivate the pursuit of the phase curves, as they will provide preliminary atmospheric characterization and mass estimation for many of the systems without investing any additional resources.

**Acknowledgments:** This work includes data taken by *K2*, and the final detrended light curves from *K2SFF* as well as *EVEREST* pipeline. Authors would like to thank Dr. Andrew Vanderburg for discussion on *K2SFF* pipeline products and kindly providing the detrended lightcurve of K2-141b. The authors would also like to thank Dr. Rodrigo Luger in regards to discussion on *EVEREST* pipeline. Authors would also like to thank the anonymous referee for insightful comments. P. Niraula acknowledges the support of the Grayce B. Kerr Fellowship Fund. at MIT. S. Redfield and P. Niraula acknowledge support from the National Science Foundation through the Astronomy and Astrophysics Research Grant AST-1313268. D. Serindag acknowledges support from the European Research Council under the European Union's Horizon 2020 research and innovation program under grant agreement No. 694513. D. Serindag also acknowledges the Undergraduate Research Fellowship awarded by the NASA CT Space Grant Consortium in support of this research.

*Software:* `batman` (Kreidberg 2015), `emcee` (Foreman-Mackey et al. 2013), `gatspy` (VanderPlas & Ivezić 2015), `lmfit` (Newville et al. 2016), `matplotlib` (Hunter 2007).

## REFERENCES

- Adams, A. D., & Laughlin, G. 2018, *AJ*, 156, 28  
 Adams, E. R., Jackson, B., Endl, M., et al. 2017, *AJ*, 153, 82  
 Angelo, I., & Hu, R. 2017, *AJ*, 154, 232  
 Angerhausen, D., DeLarme, E., & Morse, J. A. 2015, *PASP*  
 Angus, R., Foreman-Mackey, D., & Johnson, J. A. 2016, *ApJ*, 818, 109  
 Aranzana, E., K rding, E., Uttley, P., Scaringi, S., & Bloemen, S. 2018, *MNRAS*, 476, 2501  
 Armstrong, D. J., de Mooij, E., Barstow, J., et al. 2016, *Nature Astronomy*, 1, 0004  
 Baglin, A., Auvergne, M., Barge, P., et al. 2002,  
 Barclay, T., Huber, D., Rowe, J. F., et al. 2012, *ApJ*, 761, 53  
 Batalha, N. M., Borucki, W. J., Bryson, S. T., et al. 2011, *ApJ*, 729, 27  
 Bayliss, D., Hartman, J. D., Zhou, G., et al. 2018, *AJ*, 155, 119  
 Beichman, C., Benneke, B., Knutson, H., et al. 2014, *PASP*, 126, 1134  
 Borucki, W. J., Koch, D., Jenkins, J., et al. 2009, *Science*, 325, 709  
 Borucki, W. J., Koch, D., Basri, G., et al. 2010, *Science*, 327, 977  
 Brahm, R., Jord n, A., Hartman, J. D., et al. 2015, *AJ*, 150, 33  
 Broeg, C., Fortier, A., Ehrenreich, D., et al. 2013, *European Physical Journal Web of Conferences*, 47, 03005  
 Bryan, M. L., Alsubai, K. A., Latham, D. W., et al. 2012, *ApJ*, 750, 84  
 Claret, A., & Bloemen, S. 2011, *A&A*, 529, A75  
 Cowan, N. B., Chayes, V., Bouffard,  ., Meynig, M., & Haggard, H. M. 2017, *MNRAS*, 467, 747  
 Dai, F., Winn, J. N., Gandolfi, D., et al. 2017, *AJ*, 154, 226  
 Dai, F., Winn, J. N., Yu, L., & Albrecht, S. 2017, *AJ*, 153, 40  
 Demory, B.-O., de Wit, J., Lewis, N., et al. 2013, *ApJL*, 776, L25  
 Demory, B.-O., Gillon, M., de Wit, J., et al. 2016, *Nature*, 532, 207  
 de Wit, J., Lewis, N. K., Knutson, H. A., et al. 2017, *ApJL*, 836, L17  
 Dyudina, U., Zhang, X., Li, L., et al. 2016, *ApJ*, 822, 76  
 Eigm ller, P., Csizmadia, S., Endl, M., et al. 2018, *MNRAS*, 480, 3864  
 Eigm ller, P., Gandolfi, D., Persson, C. M., et al. 2017, *AJ*, 153, 130  
 Esselstein, R., Aigrain, S., Vanderburg, A., et al. 2018, *ApJ*, 859, 167  
 Esteves, L. J., De Mooij, E. J. W., & Jayawardhana, R. 2013, *ApJ*, 772, 51  
 Esteves, L. J., De Mooij, E. J. W., & Jayawardhana, R. 2015, *ApJ*, 804, 150  
 Faigler, S., Kull, I., Mazeh, T., et al. 2015, *ApJ*, 815, 26  
 Faigler, S., & Mazeh, T. 2015, *ApJ*, 800, 73  
 Faigler, S., Mazeh, T., Quinn, S. N., Latham, D. W., & Tal-Or, L. 2012, *ApJ*, 746, 185  
 Faigler, S., Tal-Or, L., Mazeh, T., Latham, D. W., & Buchhave, L. A. 2013, *ApJ*, 771, 26

- Foreman-Mackey, D., Hogg, D. W., Lang, D., & Goodman, J. 2013, *PASP*, 125, 306
- Gelman, S. E., Elkins-Tanton, L. T., & Seager, S. 2011, *ApJ*, 735, 72
- Gilliland, R. L., Chaplin, W. J., Dunham, E. W., et al. 2011, *ApJS*, 197, 6
- Grziwa, S., Gandolfi, D., Csizmadia, S., et al. 2016, *AJ*, 152, 132
- Guenther, E. W., Barragán, O., Dai, F., et al. 2017, *A&A*, 608, A93
- Handberg, R., & Lund, M. N. 2014, *MNRAS*, 445, 2698
- Harrington, J., Hansen, B. M., Luszcz, S. H., et al. 2006, *Science*, 314, 623
- Hermes, J. J., Gänsicke, B. T., Kawaler, S. D., et al. 2017, *ApJS*, 232, 23
- Hidalgo, D., Alonso, R., & Palle, E. 2018, arXiv:1810.07495
- Howell, S. B., Sobeck, C., Haas, M., et al. 2014, *PASP*, 126, 398
- Huang, C. X., Shporer, A., Dragomir, D., et al. 2018, arXiv:1807.11129
- Huang, C. X., Hartman, J. D., Bakos, G. Á., et al. 2015, *AJ*, 150, 85
- Huber, K. F., Czesla, S., & Schmitt, J. H. M. M. 2017, *A&A*, 597, A113
- Hunter, J. D. 2007, *Computing in Science and Engineering*, 9, 90
- Jackson, B., Barnes, R., & Greenberg, R. 2008, *MNRAS*, 391, 237
- Jansen, T., & Kipping, D. 2018, *MNRAS*, 478, 3025
- Jenkins, J. M., Caldwell, D. A., Chandrasekaran, H., et al. 2010, *ApJL*, 713, L87
- Johnson, M. C., Dai, F., Justesen, A. B., et al. 2018, *MNRAS*, 481, 596
- Knutson, H. A., Charbonneau, D., Allen, L. E., et al. 2007, *Nature*, 447, 183
- Kreidberg, L., Bean, J. L., Désert, J.-M., et al. 2014, *Nature*, 505, 69
- Kreidberg, L. 2015, *PASP*, 127, 1161
- Libralato, M., Nardiello, D., Bedin, L. R., et al. 2016, *MNRAS*, 463, 1780
- Lillo-Box, J., Barrado, D., Henning, T., et al. 2014, *A&A*, 568, L1
- Loeb, A., & Gaudi, B. S. 2003, *ApJL*, 588, L117
- López-Morales, M., & Seager, S. 2007, *ApJL*, 667, L191
- Luger, R., Agol, E., Kruse, E., et al. 2016, *AJ*, 152, 100
- Luger, R., Kruse, E., Foreman-Mackey, D., Agol, E., & Saunders, N. 2018, *AJ*, 156, 99
- Lund, M. N., Chaplin, W. J., Casagrande, L., et al. 2016, *PASP*, 128, 124204
- Malavolta, L., Mayo, A. W., Loudon, T., et al. 2018, *AJ*, 155, 107
- Mandel, K., & Agol, E. 2002, *ApJL*, 580, L171
- Maxted, P. F. L., Serenelli, A. M., & Southworth, J. 2015, *A&A*, 575, A36
- Millholland, S., & Laughlin, G. 2017, *AJ*, 154, 83
- Morris, S. L. 1985, *ApJ*, 295, 143
- Močnik, T., Hellier, C., Anderson, D. R., Clark, B. J. M., & Southworth, J. 2017, *MNRAS*, 469, 1622
- Močnik, T., Hellier, C., & Southworth, J. 2018, arXiv:1804.05334
- Newville, M., Stensitzki, T., Allen, D. B., et al. 2016, *Astrophysics Source Code Library*, ascl:1606.014
- Parmentier, V., & Crossfield, I. J. M. 2018, *Handbook of Exoplanets*, 116
- Peale, S. J., Cassen, P., & Reynolds, R. T. 1979, *Lunar and Planetary Science Conference*, 10, 964
- Pfahl, E., Arras, P., & Paxton, B. 2008, *ApJ*, 679, 783
- Placek, B., Knuth, K. H., & Angerhausen, D. 2016, *PASP*, 128, 074503
- Quintana, E. V., Rowe, J. F., Barclay, T., et al. 2013, *ApJ*, 767, 137
- Rabus, M., Jordán, A., Hartman, J. D., et al. 2016, *AJ*, 152, 88
- Rauer, H., Catala, C., Aerts, C., et al. 2014, *Experimental Astronomy*, 38, 249
- Ricker, G. R., Winn, J. N., Vanderspek, R., et al. 2015, *Journal of Astronomical Telescopes, Instruments, and Systems*, 1, 014003
- Sanchis-Ojeda, R., Rappaport, S., Pallè, E., et al. 2015, *ApJ*, 812, 112
- Sanchis-Ojeda, R., Rappaport, S., Winn, J. N., et al. 2013, *ApJ*, 774, 54
- Serrano, L. M., Barros, S. C. C., Oshagh, M., et al. 2018, *A&A*, 611, A8
- Sing, D. K., Fortney, J. J., Nikolov, N., et al. 2016, *Nature*, 529, 59
- Shporer, A. 2017, *PASP*, 129, 072001
- Shporer, A., & Hu, R. 2015, *AJ*, 150, 112
- Shporer, A., O'Rourke, J. G., Knutson, H. A., et al. 2014, *ApJ*, 788, 92
- Shporer, A., Wong, I., Huang, C. X., et al. 2018, arXiv:1811.06020
- Sinukoff, E., Howard, A. W., Petigura, E. A., et al. 2017, *AJ*, 153, 271
- Smith, A. M. S., Anderson, D. R., Armstrong, D. J., et al. 2014, *A&A*, 570, A64
- Smith, A. M. S., Cabrera, J., Csizmadia, S., et al. 2018, *MNRAS*, 474, 5523
- Tinetti, G., Drossart, P., Eccleston, P., et al. 2016, *Proc. SPIE*, 9904, 99041X
- Van Cleve, J. E., Howell, S. B., Smith, J. C., et al. 2016, *PASP*, 128, 075002
- Vanderburg, A., & Johnson, J. A. 2014, *PASP*, 126, 948
- Vanderburg, A., Latham, D. W., Buchhave, L. A., et al. 2016, *ApJS*, 222, 14
- VanderPlas, J. T., & Ivezić, Ž. 2015, *ApJ*, 812, 18
- Welsh, W. F., Orosz, J. A., Seager, S., et al. 2010, *ApJL*, 713, L145
- White, T. R., Pope, B. J. S., Antoci, V., et al. 2017, *MNRAS*, 471, 2882
- Winn, J. N. 2010, arXiv:1001.2010

## APPENDIX

The light curve of the six targets, where phase curve have been detected, are presented here. The cyan line represents the filtered light curve which was used to extract the phase curves. For K2-141b we use the light curve provided by Dr. Andrew Vanderburg which was used in their paper. For the rest of the eight cases, we use the light curve either from EVEREST or K2SFF as noted in their respective tables.

